Local spots of viscous electron flow in graphene at room temperature and moderate mobility

Sayanti Samaddar,[†] Jeff Strasdas,[†] Kevin Janßen,[†,‡] Tjorven Johnsen,[†] Zhenxing Wang,[¶] Daniel Neumaier,[§,¶] Marcus Liebmann,[†] and Markus Morgenstern[*,†]

[†]*2nd Institute of Physics B and JARA-FIT, RWTH Aachen University, Otto-Blumenthal-Straße, 52074 Aachen, Germany*

[‡]*Peter Grünberg Institute 6 & 9, Forschungszentrum Jülich GmbH, 52425 Jülich, Germany*

[¶]*Advanced Microelectronic Center Aachen (AMICA), AMO GmbH, Otto-Blumenthal-Str. 25, 52074 Aachen, Germany*

[§]*University of Wuppertal, 42285 Wuppertal, Germany*

E-mail: mmorgens@physik.rwth-aachen.de

April 21, 2024

Abstract

Dominating electron-electron scattering enables viscous electron flow exhibiting hydrodynamic current density patterns such as Poiseuille profiles or vortices. The viscous regime has recently been observed in graphene by non-local transport experiments and mapping of Poiseuille profiles up to room temperature. Here, we probe the current-induced surface potential maps of graphene field effect transistors using scanning probe microscopy at room temperature. We discover the appearance of μm large areas close to charge neutrality, where the current induced electric field opposes the externally applied field. By estimating the scattering lengths from the gate dependence of local

electric fields, we find that these areas exhibit a dominating electron-electron scattering as expected for viscous flow. We map the respective meandering electric fields and carefully rule out artifacts such as by source-drain voltage induced local doping. Our results imply that viscous electron flow is omnipresent in graphene devices, even at moderate mobility.

Introduction

Since electron-electron scattering is momentum conserving, if Umklapp scattering is suppressed, the corresponding electric resistance is not related to momentum relaxation, but to viscous properties of the electron liquid.[1–3] Indeed, Navier-Stokes type equations have been employed at dominating electron-electron scattering to calculate resistance and charge flow patterns.[1,4–6] Most notably, it has been shown that the resistance of a constriction can drop below its ballistic Landauer-Büttiker-type value via lateral drag as dubbed the Gurzhi effect,[7,8] that a Poisseuile flow implying an inverted parabolic velocity profile appears across a ribbon[6,9–11] and that vortices of current flow can develop[12] sideways from a current injection point[6,13–17] or within a disorder potential.[18,19] Vortices at current injection points develop also without a dominating viscous flow and are, hence, not a smoking gun.[15,20]

Experimentally, first evidence of the Gurzhi effect has been found for GaAs constrictions.[21] More recently, indications of a dominating viscous electron flow appeared in other 2D materials such as graphene[22–30] or $PdCoO_2$[31] as well as in the 3D Dirac- and Weyl-type materials $PtSn_4$[32] and WP_2,[33] respectively. These encouraging results using electric or heat transport experiments, partly at optical frequencies,[25,34] revealed the viscous flow indirectly via its detailed parameter dependence. A real-space visualization has been accomplished for graphene displaying the Poiseuille charge flow profile[35] up to room temperature[36] and its transition to ohmic[37] or ballistic transport profiles.[35] Moreover, a GaAs constriction in the viscous regime has been probed by scanning gate microscopy without conclusive interpreta-

tion of the observed patterns.[38]

Here, we employ Kelvin probe force microscopy (KPFM)[39] and electrostatic force microscopy (EFM)[40] under current flow as previously applied to static graphene at ambient conditions.[41–44] To tune the charge carrier density, we use a backgate voltage V_{gate} that is sufficiently screened to avoid a direct influence onto the probing cantilever. This enables us to map the current induced electric potentials at different V_{gate} and source-drain voltages V_{SD}. Surprisingly, we find areas, where the local potential drop opposes the externally applied V_{SD}. Such areas appear increasingly, if the sample is tuned towards charge neutrality, i.e., the Dirac point voltage V_{D}. One explanation is a novel artifact in KPFM and EFM, that we discovered during this study and dub source-drain voltage induced local doping (SDILD). Its effect including opposing fields can be quantitatively deduced from the measured map of electron concentration and, hence, identified. For the remaining areas of inverted potential drops, we use the gate dependence of the measured potentials to estimate a local electron-disorder scattering length l_{dis} that turns out to be larger than the local electron-electron scattering length l_{ee} for charge carrier densities up to about $\pm 5 \cdot 10^{16}/\mathrm{m}^2$ around V_{D}. Thus, consistently, areas of relatively short l_{ee} exhibit inverted lateral electric fields as expected in the hydrodynamic regime.[1,17,22,30,45] Since the sample exhibits a moderate mobility $\mu = 2500 - 4000\,\mathrm{cm}^2/\mathrm{Vs}$ and the effects are observed at 300 K, our results imply that viscous electron flow is ubiquitous in graphene devices.

Results and discussion

We use a graphene monolayer (Graphenea SE) deposited on a Si(100)/SiN(150 nm) backgate with source and drain electrodes (Ni/Al (12/50 nm)) structured via optical lithography (Supplementary Section 1).[46] The large drain contact (Fig. 1a), set to ground during all measurements, protects the cantilever from direct influences of V_{gate}. A commercial atomic

force microscope (Bruker Dimensions Icon PT) enables EFM and KPFM with lateral resolution down to 20 nm, while varying, both, V_{gate} and V_{SD}. Both methods are applied in lift mode. Firstly, one records a tapping mode image of the surface with cantilever amplitude of 30–33 nm. Afterwards, the average tip-sample distance is increased by $z_{\mathrm{tip}} \approx 30\,\mathrm{nm}$ to determine maps of the contact potential difference $V_{\mathrm{CPD}}(x,y) = W_{\mathrm{tip}} - W_{\mathrm{sample}}(x,y)$. Here, W_{tip} and $W_{\mathrm{sample}}(x,y)$ are the work function of the tip and of the sample area below the tip at position (x,y), respectively. Thus, both methods map the surface potential of graphene. At $V_{\mathrm{SD}} = 0\,\mathrm{V}$, it is directly related to the charge carrier density $n_0(x,y)$, i.e., the density of excess electrons with respect to charge neutrality. Deducing $n_0(x,y)$ from $V_{\mathrm{CPD}}(x,y)$ requires the contact potential difference V^0_{CPD} at charge neutrality.[47,48] This is determined straightforwardly by tuning V_{gate} to charge neutrality, i.e., to the maximum of two-point resistance as function of V_{gate} (Fig. 1e) (Supplementary Section 5).

In EFM, one drives the cantilever at frequency f_{drive} slightly below the resonance frequency of the free cantilever ($\sim 62\,\mathrm{kHz}$) and detects the phase lag ϕ_{EFM} of the excitation with respect to the cantilever oscillation. The resulting ϕ_{EFM} as function of tip voltage V_{tip} features an inverted parabola $\phi_{\mathrm{EFM}}(V_{\mathrm{tip}})$ (Fig. 1b). This is due to the cantilever softening that is caused by the attractive electrostatic interaction between the charged tip and the induced charge within the sample. The maximum of the parabola is, hence, at vanishing electrostatic force, i.e., at $V_{\mathrm{tip}} = V_{\mathrm{CPD}}$.[40] To obtain $V_{\mathrm{CPD}}(x,y)$ maps, it is sufficient to probe $\Delta\phi$ at three distinct V_{tip} such that the fitted parabola (Fig. 1b, black line) reveals V_{CPD} with an accuracy of about 2 mV (Supplementary Section 3.1). KPFM is faster in recording, since adapting $V_{\mathrm{tip}} = V_{\mathrm{CPD}}(x,y)$ via feedback control that minimizes electrostatic forces, but it is more prone to voltage signals from the environment such as remaining electric fields from V_{gate} penetrating to the cantilever.[40,41] This leads to a smooth background in $V_{\mathrm{CPD}}(x,y)$ images that had to be subtracted (Supplementary Section 2.2).

Figure 1c shows two measured profiles $V_{\mathrm{CPD}}(x)$ (x: lateral position) along the same line of graphene at $V_{\mathrm{SD}} = 0\,\mathrm{V}$ and $V_{\mathrm{SD}} = 0.25\,\mathrm{V}$ ($V_{\mathrm{gate}} = V_{\mathrm{D}} = 85\,\mathrm{V}$). The corresponding topography

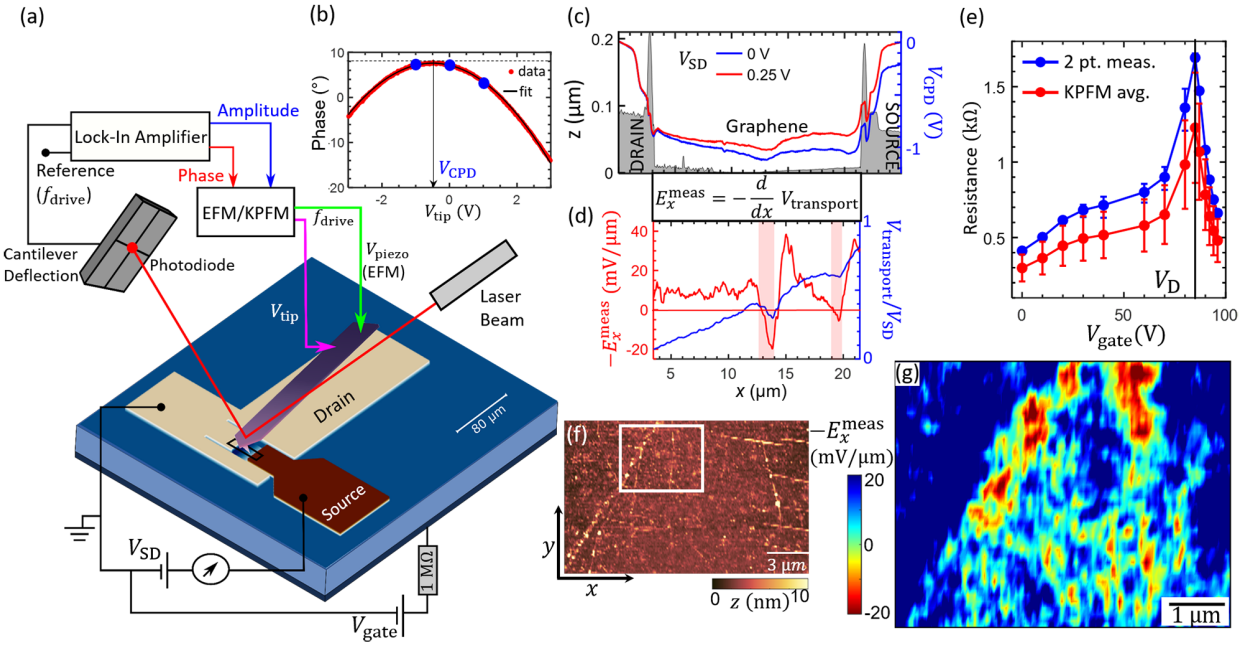

Figure 1: **Measurement scheme, sample characterization and inverted electric fields.** (a) Setup to image lateral electric fields induced by charge transport $E_x^{\mathrm{meas}}(x,y)$, V_{gate}: gate voltage, V_{SD}: source-drain voltage, V_{tip}: tip voltage, f_{drive}: drive frequency of cantilever deflection voltage $V_{\mathrm{piezo}}(t)$ for EFM and $V_{\mathrm{tip}}(t)$ for KPFM, serving as reference for lock-in detection. The large, grounded drain pad (beige) protects the cantilever (violet) from influences of V_{gate}. Cantilever size and sample geometry are roughly to scale. (b) Red: Measured phase of cantilever oscillation on graphene. Black: parabolic fit with marked, deduced contact potential difference $V_{\mathrm{CPD}} = W_{\mathrm{tip}} - W_{\mathrm{sample}}$ (V_{tip} at maximum). Blue dots: three phases probed subsequently at the same location as the red data points. Such three phases are recorded for each position (x,y) to reconstruct the full parabola and, hence, $V_{\mathrm{CPD}}(x,y)$ (Supplementary Section 3). (c) Blue, red: $V_{\mathrm{CPD}}(x)$ along the same line, but at different V_{SD}, $V_{\mathrm{gate}} = 85\,\mathrm{V}$ (charge neutrality). Grey areas: topography along the same line with graphene, source and drain electrode marked. (d) Blue: $\frac{V_{\mathrm{transport}}}{V_{\mathrm{SD}}}(x) := \frac{[V_{\mathrm{CPD}}(x,V_{\mathrm{SD}}) - V_{\mathrm{CPD}}(x,V_{\mathrm{SD}}=0\,\mathrm{V})]}{V_{\mathrm{SD}}}$ using the two $V_{\mathrm{CPD}}(x,V_{\mathrm{SD}})$ from c. Red: deduced $E_x^{\mathrm{meas}}(x)$ via the formula between c and d. Pink background highlights inverted $E_x^{\mathrm{meas}}(x)$ areas. (e) Red: Spatially averaged $\langle E_x^{\mathrm{meas}}(x,y)\rangle \cdot L/I_{\mathrm{SD}}$ representing the sample averaged resistance as probed by KPFM, $L = 18\,\mu\mathrm{m}$: graphene sample length along V_{SD}, I_{SD}: source-drain current. Blue: simultaneously measured two point resistance, V_{D}: Dirac point. (f) Topography of graphene area (tapping mode AFM). (g) $E_x^{\mathrm{meas}}(x,y)$ in the area of the white rectangle in f probed by KPFM, $V_{\mathrm{gate}} = 80\,\mathrm{V}$, $V_{\mathrm{SD}} = 500\,\mathrm{mV}$, $z_{\mathrm{tip}} = 30\,\mathrm{nm}$, amplitude of $V_{\mathrm{tip}}(t)$ for lock-in detection: $V_{\mathrm{tip,ac}} = 1.1\,\mathrm{V}$, $f_{\mathrm{drive}} = 61.34\,\mathrm{kHz}$, recording time of each $V_{\mathrm{CPD}}(x,y)$ image: 26 min.

(grey areas) reveals the positions of the Al electrodes, where $V_{\mathrm{CPD}}(x)$ exhibits a work function difference to graphene. The $V_{\mathrm{CPD}}(x)$ lines show fluctuations across the graphene, attributed to charge puddles.[49] Moreover, application of V_{SD} changes the slope of $V_{\mathrm{CPD}}(x)$ indicating the current induced potential drop. To disentangle charge puddles and current induced potential $V_{\mathrm{transport}}(x)$, we simply subtract the two curves. Dividing $V_{\mathrm{transport}}(x)$ by the applied V_{SD} reveals that about 80 % of V_{SD} drop across graphene (Fig. 1d). Notably, $V_{\mathrm{transport}}/V_{\mathrm{SD}}$ partially exhibits a negative slope (highlighted areas in Fig. 1d), i.e., an inverted voltage drop with respect to V_{SD}. The resulting in-plane electric field $E_x^{\mathrm{meas}}(x) = -dV_{\mathrm{transport}}(x)/dx$, hence, is also inverted with respect to the electric field direction caused by the the applied V_{SD} (red line, Fig. 1d). We consistently display $-E_x^{\mathrm{meas}}$ in graphs and maps such that the inverted electric fields always appear negative. The electric field inversion appears ubiquitously in maps of $E_x^{\mathrm{meas}}(x, y)$ if recorded close to charge neutrality, i.e., at $V_{\mathrm{gate}} \simeq V_{\mathrm{D}} \pm 15\,\mathrm{V}$ (Fig. 1g). Areas of inverted $E_x^{\mathrm{meas}}(x, y)$ are partly correlated with topographic features as at the diagonal fold starting at the lower left in the topography map (Fig. 1f), where multiple inverted $E_x^{\mathrm{meas}}(x, y)$ areas appear on its right (Fig. 1g, see also Fig. 5). We crosschecked that the simultaneously recorded two-point resistance $R_{\mathrm{transport}}$ agrees with the gate dependence of the spatially averaged $E_x^{\mathrm{meas}}(x, y)$ after adequate scaling (Fig. 1e). The data nicely match except of a small difference of 80-160 Ω that is nearly the same as the metal-graphene contact resistance revealed by 4-point measurements of identically prepared samples.[46]

The inverted electric fields with respect to V_{SD} (Fig. 1g) imply a complex charge redistribution by the current flow. Such charge redistribution is known to appear in the hydrodynamic regime, e.g., via current vortices.[1] Hence, it is tempting to assume that the inverted $E_x^{\mathrm{meas}}(x, y)$ is due to viscous electron flow.[1–3]

However, there is an artifact leading to an apparent inverted $E_x^{\mathrm{meas}}(x, y)$ at $V_{\mathrm{gate}} \simeq V_{\mathrm{D}}$. It results from the local doping change by the applied V_{SD}[29] (Fig. 2a) and has to be carefully distinguished from a current induced inverted $E_x^{\mathrm{meas}}(x, y)$. To understand the artifact, we

firstly recall that $E_x^{\mathrm{meas}}(x,y)$ at given V_{SD} is determined from recorded $V_{\mathrm{CPD}}(x,y)$ maps via

$$E_x^{\mathrm{meas}}(x,y) = -\frac{d(V_{\mathrm{CPD}}(x,y,V_{\mathrm{SD}}) - V_{\mathrm{CPD}}(x,y,V_{\mathrm{SD}}=0))}{dx} \tag{1}$$

.

Assuming that the applied V_{SD} drops rigidly linear across the graphene, one straightforwardly obtains (Supplementary Section 6, eq. (S16))

$$E_x^{\mathrm{meas}}(x,y) = -\frac{V_{\mathrm{SD}}}{L} - \frac{\hbar v_{\mathrm{F}}\sqrt{\pi}}{2|e|}\left(\frac{1}{\sqrt{|n(x,y)|}}\frac{dn(x,y)}{dx} - \frac{1}{\sqrt{|n_0(x,y)|}}\frac{dn_0(x,y)}{dx}\right) := E_x^{\mathrm{SDILD}}(x,y). \tag{2}$$

Here, $L = 18.5\,\mu$m is the length of V_{SD} drop, $v_{\mathrm{F}} \simeq 10^6\,$m/s is graphene's Fermi velocity and $n(x,y)$ ($n_0(x,y)$) is the charge carrier density at applied V_{SD} (without V_{SD}). We include quantum capacitance to calculate $n(x,y)$, $n_0(x,y)$ (Supplementary Section 5). The field is dubbed $E_x^{\mathrm{SDILD}}(x,y)$ with SDILD abbreviating source-drain voltage induced local doping. Obviously, $E_x^{\mathrm{SDILD}}(x,y)$ diverges at $n(x,y) = 0$ and $n_0(x,y) = 0$ with sign depending on the spatial derivative of the corresponding charge carrier density, and being opposite for $n(x,y)$ and $n_0(x,y)$. After normalizing $E_x^{\mathrm{SDILD}}(x,y)$ to V_{SD} for easier comparison (analogously $E_x^{\mathrm{meas}}(x,y)$):

$$\widehat{E}_x^{\mathrm{SDILD}}(x,y) = \frac{E_x^{\mathrm{SDILD}}(x,y)}{V_{\mathrm{SD}}}, \qquad \widehat{E}_x^{\mathrm{meas}}(x,y) = \frac{E_x^{\mathrm{meas}}(x,y)}{V_{\mathrm{SD}}}, \tag{3}$$

the sign of the divergence also depends on the sign of V_{SD}.

Since V_{SD} necessarily shifts the zero crossings of the charge carrier density along x, parallel to V_{SD}, (Fig. 2b) one usually gets two divergences of opposite sign (Fig. 2c), one at $n_0(x) = 0$ ($V_{\mathrm{SD}} = 0$) and one at the shifted $n(x) = 0$ ($V_{\mathrm{SD}} \neq 0$). As a result, most of the $n_0(x) = 0$ points feature a double divergence of $\widehat{E}_x^{\mathrm{SDILD}}(x)$ in opposite directions (Fig. 2c). Figure 2b and c show an example for an electron puddle $n_0(x)$ with diameter $1.4\,\mu$m embedded into a hole density. The puddle implies two zero crossing $n_0(x) = 0$ (Fig. 2b). Tilting the

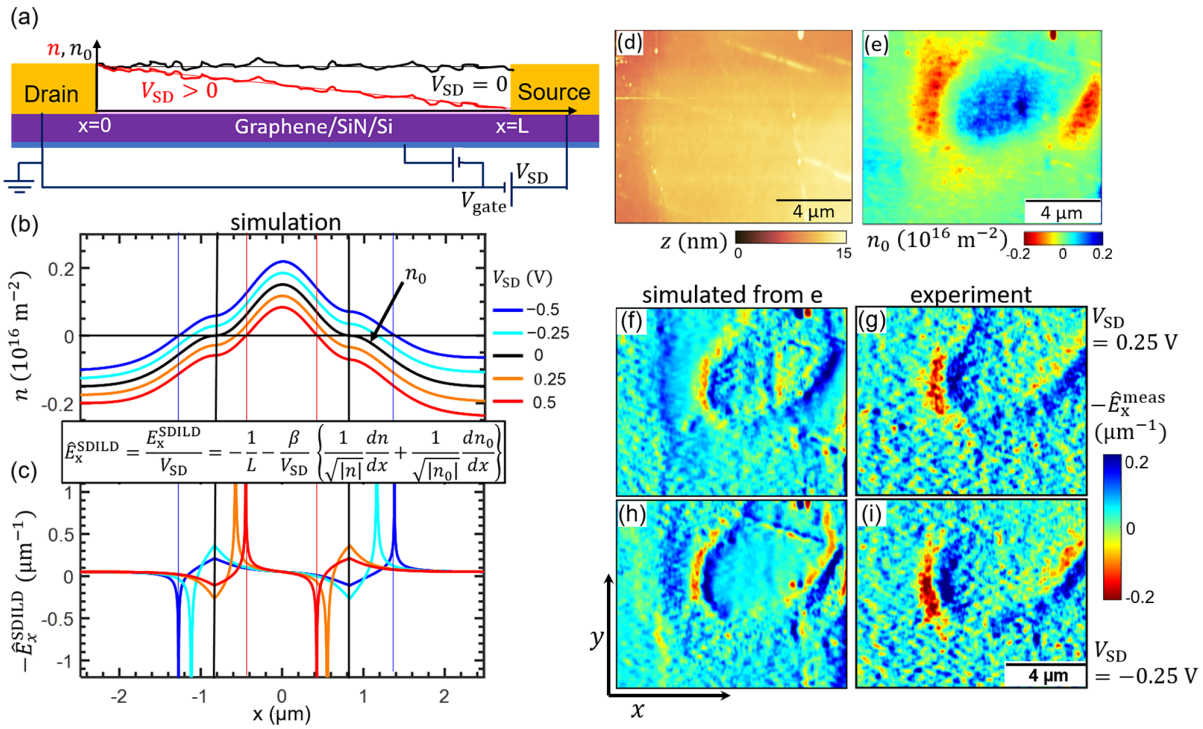

Figure 2: **Inverted $\widehat{E}_x^{\mathrm{meas}}(x)$ by source-drain voltage induced local doping (SDILD).** (a) Sample sketch with exemplary charge carrier density $n_0(x)$ (black line, $V_{\mathrm{SD}} = 0\,\mathrm{V}$) and resulting $n(x)$ (red line, $V_{\mathrm{SD}} > 0\,\mathrm{V}$). Thin lines: $n_0(x)$, $n(x)$ without charge puddles. (b) Smaller scale of $n_0(x)$, $n(x)$ for multiple V_{SD}, $V_{\mathrm{gate}} \simeq V_{\mathrm{D}}$. The $n_0(x)$ profile (black, $V_{\mathrm{SD}} = 0\,\mathrm{V}$) corresponds to a Gaussian shaped potential that crosses E_{F}, i.e., an electron puddle surrounded by holes. Vertical lines: positions of $n_0(x) = 0$ (black) and $n(x) = 0$ (colored). (c) $\widehat{E}_x^{\mathrm{SDILD}}(x)$ deduced from b according to eq. (2), (3) as indicated between b and c ($\beta = \hbar v_{\mathrm{D}}\sqrt{\pi}/2|e|$). (d) Graphene topography (tapping mode AFM). (e) Equilibrium doping $n_0(x, y)$ of the same area as in d, deduced from $V_{\mathrm{CPD}}(x, y, V_{\mathrm{SD}} = 0)$ as recorded by KPFM, $V_{\mathrm{gate}} = V_{\mathrm{D}} = 85\,\mathrm{V}$. (f), (h) $\widehat{E}_x^{\mathrm{SDILD}}(x, y)$ deduced from $n_0(x, y)$ of e via eq. (2), (3) after tilting $V_{\mathrm{CPD}}(x, y, V_{\mathrm{SD}} = 0)$ to get $n(x, y)$ according to eq. (S14) (Supplementary Section 5.1) at $V_{\mathrm{SD}} \neq 0\,\mathrm{V}$ as marked on the right of g, i. (g), (i) Measured $\widehat{E}_x^{\mathrm{meas}}(x, y)$ at the same V_{SD} as f, h. (e), (g), (i) $z_{\mathrm{tip}} = 30\,\mathrm{nm}$, $V_{\mathrm{ac}} = 1.1\,\mathrm{V}$, $f_{\mathrm{drive}} = 61.355\,\mathrm{kHz}$, $V_{\mathrm{CPD}}(x, y)$ image sequence (V_{SD} (waiting time/recording time)): -0.25 V (5'/22') → 0 V (5'/22') → 0.25 V (5'/22').

$n_0(x)$ profile by V_{SD} shifts the zero crossings laterally (Fig. 2b). The resulting $\widehat{E}_x^{\mathrm{SDILD}}(x)$ for $V_{\mathrm{SD}} > 0\,\mathrm{V}$ (Fig. 2c, orange/red line) shows a negative dip for the left position $n_0(x) \simeq 0$ (left vertical black line) due to positive slope $dn_0(x)/dx$. The shifted $n(x) = 0$ (larger positive slope) exhibits a sharper, but positive bump shifted to the right. Consistently, the signs of the (virtual) divergences are inverted by changing either the sign of V_{SD} or the sign of $dn_0(x)/dx$, e.g., at $x \simeq 1.4\,\mu\mathrm{m}$ in Fig. 2b, c. The divergences are naturally softened by the finite raster size avoiding a precise $n_0(x) = 0$.

The SDILD effect is indeed observed in the experiment. Figure 2d shows the topography and Fig. 2e the $n_0(x, y)$ map deduced from $V_{\mathrm{CPD}}(x, y, V_{\mathrm{SD}} = 0\,\mathrm{V})$ recorded at $V_{\mathrm{gate}} = V_{\mathrm{D}}$. An electron puddle of size $5\,\mu\mathrm{m}$ is apparent with amplitude $2 \times 10^{11}/\mathrm{cm}^2$. Figure 2f, h display the resulting $\widehat{E}_x^{\mathrm{SDILD}}(x, y)$ for two opposite V_{SD} using eq. (2), (3) and calculating $n(x, y)$ by tilting the potential and including quantum capacitance (Supplementary Section 5.1, eq. (S14)). The $\widehat{E}_x^{\mathrm{meas}}(x, y)$ maps recorded by measurement of $V_{\mathrm{CPD}}(x, y, V_{\mathrm{SD}})$ and using eq. (1) are displayed in Fig. 2g, i. The latter include both, current induced electric fields and SDILD effects. Obviously, most details of the experiment are reproduced by the simulation revealing that the apparent inverted $\widehat{E}_x^{\mathrm{meas}}(x, y)$ (red areas) is induced by SDILD and not by a spatially inhomogeneous current flow. Thus, one must distinguish SDILD artifacts from real current induced inverted $\widehat{E}_x^{\mathrm{meas}}(x, y)$.

Figure 3 shows an example, where this has been accomplished. Figure 3a displays the charge carrier density $n_0(x, y)$ deduced from $V_{\mathrm{CPD}}(x, y, V_{\mathrm{SD}} = 0\,\mathrm{V})$. Figure 3c displays the resulting $\widehat{E}_x^{\mathrm{SDILD}}(x, y)$ at $V_{\mathrm{SD}} = 0.1\,\mathrm{V}$ according to eq. (2) and (3), and Fig. 3e the measured $\widehat{E}_x^{\mathrm{meas}}(x, y)$ at the same V_{SD}. The $\widehat{E}_x^{\mathrm{meas}}(x, y)$ map features an extended dipolar structure (total width: $\sim 4\,\mu\mathrm{m}$) consisting of two lobes with opposite fields having the inverted electric fields on the left (Fig. 3e). In contrast, the weak dipolar structure of $\widehat{E}_x^{\mathrm{SDILD}}(x, y)$ is a factor of ten smaller in amplitude (color bars), a factor of four smaller in x extension and has the wrong order with inverted field on the right (Fig. 3c). Since the doping profile $n_0(x, y)$ temporarily fluctuates at ambient conditions, we firstly minimized these fluctuations by adequate waiting

times prior to the $V_{\mathrm{CPD}}(x,y)$ recording and by optimizing the sequences to change V_{SD} and V_{gate} (Supplementary Section 4.2, Fig. S8). Moreover, we recorded $V_{\mathrm{CPD}}(x,y,V_{\mathrm{SD}}=0\,\mathrm{V})$ prior and after $V_{\mathrm{CPD}}(x,y,V_{\mathrm{SD}}\neq 0\,\mathrm{V})$ (eq. (1)). The resulting two image sets consisting of $n_0(x,y)$, $\widehat{E}_x^{\mathrm{SDILD}}(x,y)$, and $\widehat{E}_x^{\mathrm{meas}}(x,y)$ are compared in Fig. 3 revealing that the small changes in $n_0(x,y)$ (Fig. 3a, b) barely change the dipolar structure of $\widehat{E}_x^{\mathrm{meas}}(x,y)$ (Fig. 3e, f) that in both cases strongly deviates from $\widehat{E}_x^{\mathrm{SDILD}}(x,y)$ (Fig. 3c, d).

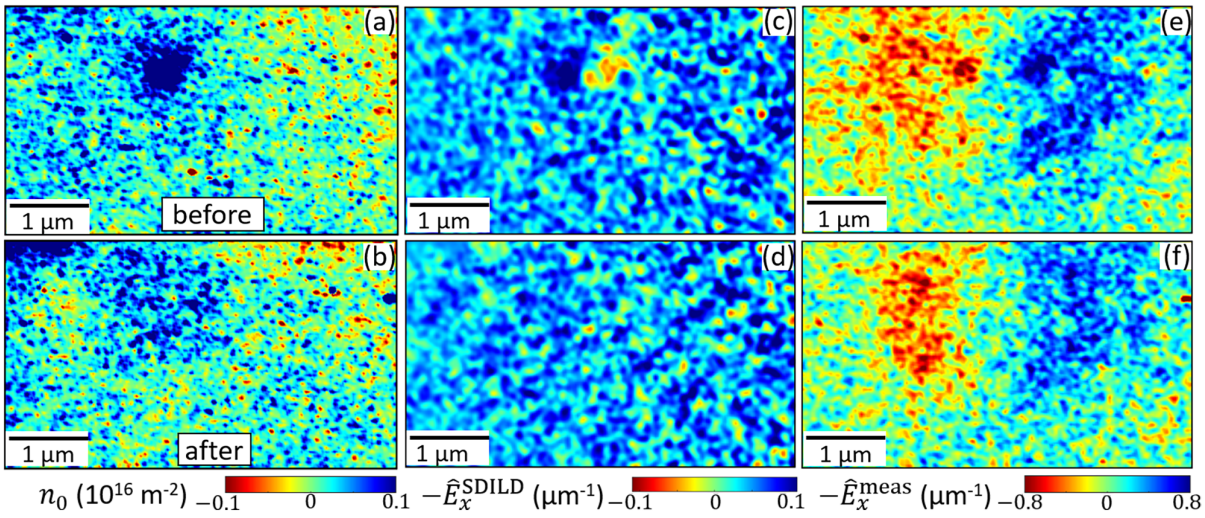

Figure 3: **Current induced inverted electric fields not caused by $\widehat{E}_x^{\mathrm{SDILD}}$.** (a), (b) Graphene doping maps $n_0(x,y)$ as deduced from $V_{\mathrm{CPD}}(x,y,V_{\mathrm{SD}}=0V)$ recorded by EFM. Both images display the same sample area, but are recorded prior (a) and after (b) recording $V_{\mathrm{CPD}}(x,y,V_{\mathrm{SD}}=0.1\,\mathrm{V})$ to determine $\widehat{E}_x^{\mathrm{meas}}(x,y)$, $V_{\mathrm{gate}}=V_{\mathrm{D}}=85\,\mathrm{V}$, $z_{\mathrm{tip}}=20\,\mathrm{nm}$, $f_{\mathrm{drive}}=61.72\,\mathrm{kHz}$, cantilever amplitude: $A=31\,\mathrm{nm}$, recording time/image: 34 min. (c), (d) $\widehat{E}_x^{\mathrm{SDILD}}(x,y)$ deduced from a, b, respectively, using eqs. (2), (3) and $V_{\mathrm{SD}}=0.1\,\mathrm{V}$. (e), (f) $\widehat{E}_x^{\mathrm{meas}}(x,y)$ at $V_{\mathrm{SD}}=0.1\,\mathrm{V}$ via eq. (1) employing $V_{\mathrm{CPD}}(x,y,V_{\mathrm{SD}}=0\,\mathrm{V})$ from a, b, respectively, as recorded $\sim 90\,\mathrm{min}$ after (a) and $\sim 30\,\mathrm{min}$ before (b) the additionally required $V_{\mathrm{CPD}}(x,y,V_{\mathrm{SD}}=0.1\,\mathrm{V})$.

Consequently, we attribute the observed dipolar $\widehat{E}_x^{\mathrm{meas}}(x,y)$ feature in Fig. 3e–f, including a large area of inverted $\widehat{E}_x^{\mathrm{meas}}(x,y)$, to a spatially inhomogeneous current flow. Inverted $\widehat{E}_x^{\mathrm{meas}}(x,y)$ areas can be rationalized by a passing current that reduces the charge carrier density in a nearby area compared to the one that would be there by SDILD only, i.e., charge puddles are sucked from the passing current without being compensated by the forward electron flow. This has been observed in simulations for viscous electron flow within a

disorder potential[1,18,30,45] where a lateral viscous force pulls electrons out of a relatively quiet area that is protected from electron flow, e.g., by an upstream obstacle.[1,14,17]

To corroborate the claim of decisive electron viscosity, we demonstrate that the puddles of inverted $\widehat{E}_x^{\mathrm{meas}}(x,y)$ indeed exhibit conditions favoring viscous current flow, namely $l_{\mathrm{ee}} < l_{\mathrm{dis}}$.[1,30] Figure 4a–f show $\widehat{E}_x^{\mathrm{meas}}(x,y)$ of graphene at various V_{gate}. Areas of inverted $\widehat{E}_x^{\mathrm{meas}}(x,y)$ appear close to $V_{\mathrm{gate}} = V_{\mathrm{D}}$, here at the electron side ($V_{\mathrm{gate}} > V_{\mathrm{D}}$). We note that the measured $n_0(x,y)$ in this area does not exhibit any zeroes at $V_{\mathrm{gate}} - V_{\mathrm{D}} \geq 3\,\mathrm{V}$, hence, SDILD is negligible. Firstly, we estimate $l_{\mathrm{ee}}(x,y)$ as local property via $n(x,y)$ deduced from the measured $n_0(x,y)$ (Supplementary Section 5.1, eq. (S14)) using[50,51]

$$l_{\mathrm{ee}}(x,y) = \frac{4}{\pi}\left(\frac{\hbar v_{\mathrm{F}}}{k_{\mathrm{B}}T}\right)^2 \left\langle \sqrt{\pi|n(x,y)|}\,\frac{1}{\ln\frac{2\hbar v_{\mathrm{F}}\sqrt{\pi|n(x,y)|}}{k_{\mathrm{B}}T}} \right\rangle \tag{4}$$

as reasonable estimate for l_{ee} within a factor of 1.5 except at $|n| < 2 \cdot 10^{14}/\,\mathrm{m}^2$ (quantum critical regime)[52,53] ($T = 298\,\mathrm{K}$: temperature, k_{B}: Boltzmann constant, $\hbar$: reduced Planck's constant).

Secondly, we determine $l_{\mathrm{dis}}(x,y)$ from the measured $E_x^{\mathrm{meas}}(x,y)$ far away from charge neutrality, where electron-electron scattering is irrelevant, using[54]

$$l_{\mathrm{dis}}(x,y) = \left(\frac{h}{2e^2}\right)\left\langle \frac{1}{\sqrt{\pi|n(x,y)|}\cdot\rho_{\mathrm{local}}(x,y)} \right\rangle. \tag{5}$$

Here, $\rho_{\mathrm{local}}(x,y) = E_x^{\mathrm{meas}}(x,y)\cdot W/I_{\mathrm{SD}}$ (e: electron charge, $W = 28\,\mu\mathrm{m}$: width of sample, I_{SD}: source-drain current) represents the local resistivity for areas where the current flow is unidirectional, as at $|V_{\mathrm{gate}} - V_{\mathrm{D}}| > 70\,\mathrm{V}$ (Fig. 5a). For consistency, we subsequently average $l_{\mathrm{ee}}(x,y)$ and $l_{\mathrm{dis}}(x,y)$ across areas larger than the scattering lengths (Supplementary Section 7).

To extrapolate $l_{\mathrm{dis}}(x,y)$ towards V_{D}, we have to deduce if short-range or long-range scattering dominates.[54] The inset in Fig. 4g shows $\langle\rho_{\mathrm{local}}(x,y)\rangle\,(V_{\mathrm{gate}} - V_{\mathrm{D}})$, averaged across a larger area of $\sim 100\,\mu\mathrm{m}^2$. The maximum is close to V_{D} as expected. More importantly,

a rather constant $\langle \rho_{\mathrm{local}}(x,y) \rangle$ appears at large hole doping indicating a dominating short-range scattering.[54] Hence, we use eq. (5) to extrapolate $\langle l_{\mathrm{dis}}(x,y) \rangle$ to $V_{\mathrm{gate}} - V_{\mathrm{D}} \simeq 0\,\mathrm{V}$ using gate independent $\rho_{\mathrm{local}}(x,y)$.[54] This formally includes the electron-phonon contribution (Supplementary Section 7.2).[54,55]

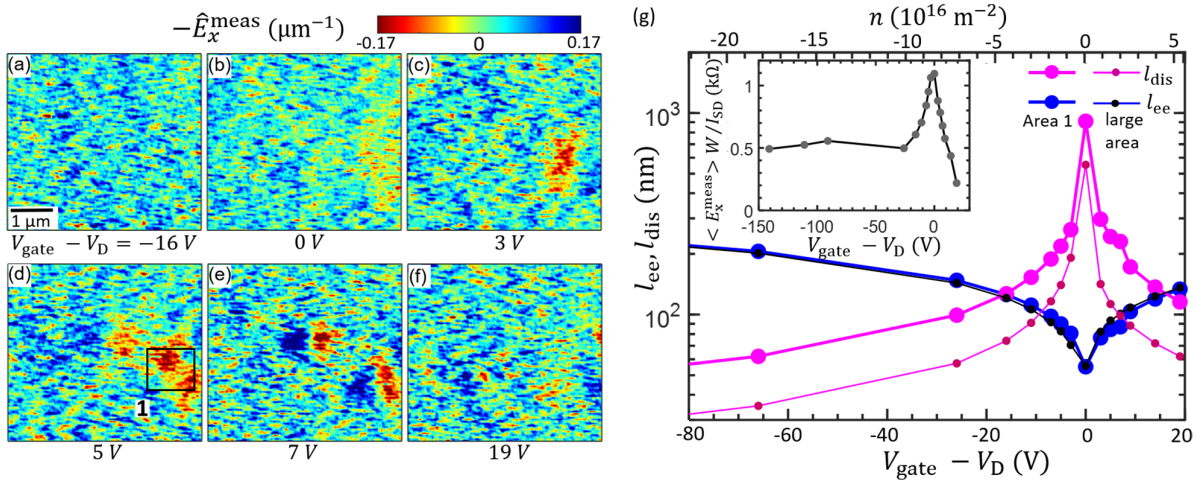

Figure 4: **Relation of inverted $E_x^{\mathrm{meas}}(x,y)$ areas to the different scattering lengths.** (a)-(f) $\widehat{E}_x^{\mathrm{meas}}(x,y)$ of a single area at different $V_{\mathrm{gate}} - V_{\mathrm{D}}$ (EFM), $V_{\mathrm{D}} = 81$ V, $z_{\mathrm{tip}} = 30$ nm, $f_{\mathrm{drive}} = 62.344$ kHz, sequence of $V_{\mathrm{CPD}}(x,y)$ images at each V_{gate} (V_{SD} (waiting time/recording time)): 0 V (5'/20') → 0.4 V (5'/20'). Black rectangle in d highlights an area of inverted $\widehat{E}_x^{\mathrm{meas}}(x,y)$. (g) Gate dependence of electron-electron scattering length l_{ee} (blue, black, eq. (4), $T = 298\,\mathrm{K}$) and electron-disorder scattering length l_{dis} (pink, eq. (5)) averaged across the black rectangle in d (large symbols) and across a larger area (12.5 μm × 8.33 μm, small symbols). The divergence in l_{dis} at $V_{\mathrm{gate}} = V_{\mathrm{D}}$ (eq. (5)) and in l_{ee} (eq. (4)) are avoided by using $n_0(x,y) = 5 \cdot 10^{14}\,\mathrm{m}^{-2}$ at V_{D} as naturally appearing by charge puddles (Figs. 2e, 3a–b). These puddle fluctuations are larger than the quantum critical limit $n_{\mathrm{QC}} = 2 \times 10^{14}$ m^{-2} [53] or the thermal limit $n_{\mathrm{Th}} = 4 \times 10^{14}$ m^{-2},[51] both principally bordering the low n applicability of eq. (5).[51] Inset: $\langle E_x^{\mathrm{meas}}(x,y) \rangle$ spatially averaged across 12.5 μm × 8.33 μm and scaled to represent the local resistivity $\langle \rho_{\mathrm{local}}(x,y) \rangle = \langle E_x^{\mathrm{meas}}(x,y) \rangle \cdot W/I_{\mathrm{SD}}$ (W: sample width). Constant resistivity appears at large hole doping and, thus, $\langle \rho_{\mathrm{local}}(x,y) \rangle$ is attributed to short-range disorder scattering.[54]

Figure 4g displays $\langle l_{\mathrm{dis}}(x,y) \rangle$ for the black rectangle area of Fig. 4d (large pink dots) and for a 100 μm^2 area (small pink dots) together with the more directly determined $\langle l_{\mathrm{ee}}(x,y) \rangle$ (eq. (4), blue, black dots). Obviously, the V_{gate} range with $l_{\mathrm{ee}} < l_{\mathrm{dis}}$ is significantly larger for the area of inverted $\widehat{E}_x^{\mathrm{meas}}(x,y)$ than for the extended area. An extended V_{gate} area with $l_{\mathrm{ee}} < l_{\mathrm{dis}}$ is consistently observed in most regions of inverted $\widehat{E}_x^{\mathrm{meas}}(x,y)$ (Supplementary Sec-

tion 7.3, Fig. S15f). Hence, the conditions for viscous electron flow are generally realized at $V_{\mathrm{gate}} \simeq V_{\mathrm{D}}$ in our sample and appear most pronounced in areas of inverted $\widehat{E}_x^{\mathrm{meas}}(x,y)$. We regard this as strong evidence that hydrodynamic electron flow indeed causes the experimentally found inverted $\widehat{E}_x^{\mathrm{meas}}(x,y)$ areas (except if attributed to SDILD). This central result is remarkable, since we operate at moderate mobility, $\mu = 2000 - 4000\,\mathrm{cm}^2/\mathrm{Vs}$, and ambient conditions similar to typical graphene devices.[56] It implies that hydrodynamic electron flow is relevant also in corresponding graphene applications.

Moreover, our results establish EFM and KPFM as commercially available methods to probe consequences of hydrodynamic electron flow with high spatial resolution.[45] This is particularly helpful for regimes, where relatively short length scales of viscous patterns prohibit their detection by negative vicinity resistance.[17,22] Moreover, EFM is significantly simpler than the more elaborate scanning probe methods as, e.g., scanning of a carbon nanotube quantum dot,[57] scanning NV centers[35–37] or scanning tunneling potentiometry.[58] Figure 5 showcases additional experimental observations highlighting the opportunities for future studies. Figure 5a−f display $\widehat{E}_x^{\mathrm{meas}}(x,y)$ of an area recorded by KPFM at different V_{gate}. Again, inverted $\widehat{E}_x^{\mathrm{meas}}(x,y)$ areas appear consistently at different V_{gate} around $V_{\mathrm{gate}} \simeq V_{\mathrm{D}}$, but, in contrast to Fig. 4a−f, on the hole side, i.e., at negative $V_{\mathrm{gate}} - V_{\mathrm{D}}$. Again, these areas cannot be attributed to SDILD by using the probed $n_0(x,y)$. Comparison with the topography of the area (Fig. 1f) reveals a strong influence of a topographic fold ($\sim 1.4\,\mathrm{nm}$ in height) on the current flow pattern. Figure 5g shows an arrow plot of the in-plane electric field $\mathbf{E}^{\mathrm{meas}}(x,y) = -\nabla V_{\mathrm{transport}}(x,y)$ at charge neutrality displayed on top of a color plot showcasing $n(x,y)$. This visualizes the correlation between local charge carrier density and current induced curvatures of $\mathbf{E}$ field patterns (Supplementary Section Fig. S6). Moreover, Fig. 5h−m demonstrate the disentangling of SDILD and current induced electric fields via comparing $\widehat{E}^{\mathrm{meas}}(x,y)$ and $\widehat{E}^{\mathrm{SDILD}}(x,y)$ of the same area. Obviously, most of the calculated SDILD patterns are reproduced by the measured $\widehat{E}^{\mathrm{meas}}(x,y)$, such that additional, more extended features can be attributed rather unambiguously to viscous electron flow. Finally,

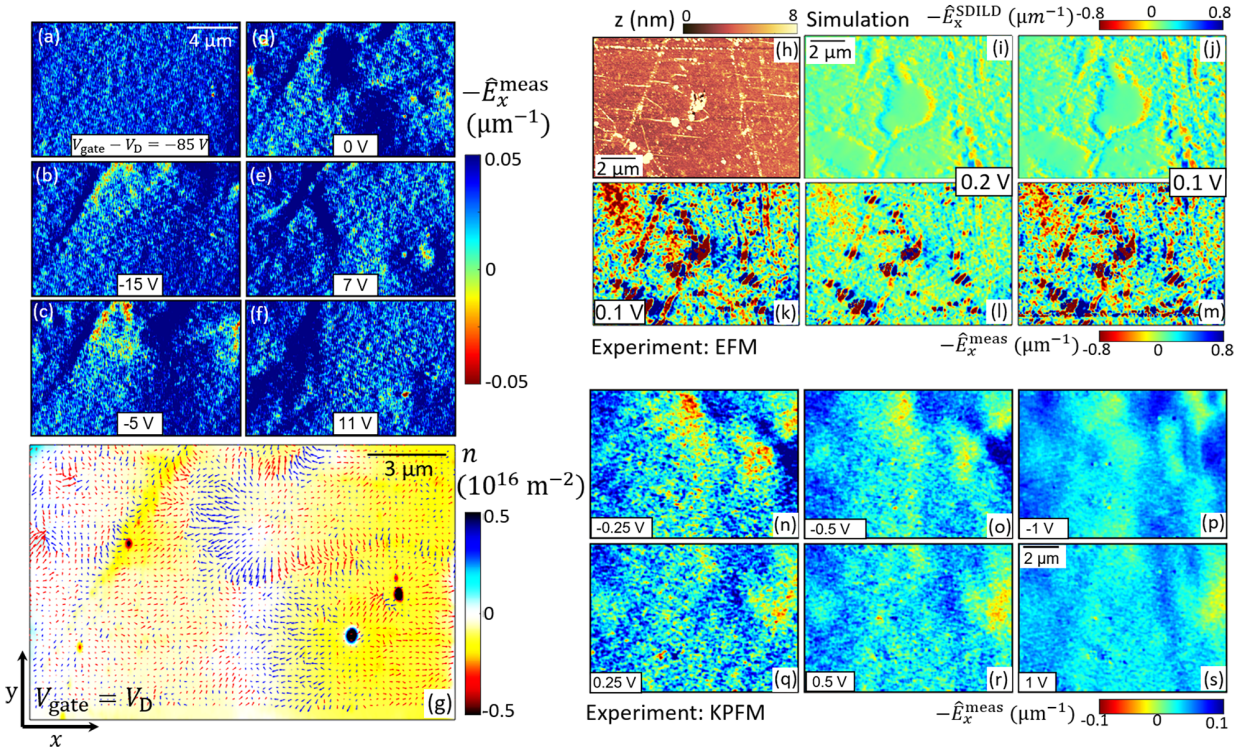

Figure 5: **Ubiquity of inverted** $\widehat{E}_x^{\mathrm{meas}}(x,y)$**.** (a)−(f) $\widehat{E}_x^{\mathrm{meas}}(x,y)$ of another graphene area recorded by KPFM, $V_{\mathrm{gate}} - V_{\mathrm{D}}$ marked, $V_{\mathrm{SD}} = 0.5\,V$, $z_{\mathrm{tip}} = 30\,\mathrm{nm}$, $f_{\mathrm{drive}} = 61.34\,\mathrm{kHz}$, $V_{\mathrm{ac}} = 1.1\,\mathrm{V}$, recording time per $V_{\mathrm{CPD}}(x,y)$ image: 21', waiting time prior to recording: 5'. (g) same as (d) in different representation: arrows: in-plane electric field vectors $\mathbf{E}^{\mathrm{meas}}(x,y) = -\nabla V_{\mathrm{transport}}(x,y)$, arrow color: blue (red): x component along (opposing) V_{SD}, background color: $n(x,y)$, a background subtraction has been applied to $V_{\mathrm{CPD}}(x,y,V_{\mathrm{SD}})$ that slightly influences $\mathbf{E}^{\mathrm{meas}}(x,y)$ (Supplementary Section 2.2, 4). (h) Topography of a different graphene area (tapping mode AFM). (i)−(j) $\widehat{E}_x^{\mathrm{SDILD}}(x,y)$ maps of the area of h deduced from $V_{\mathrm{CPD}}(x,y,V_{\mathrm{SD}} = 0\,\mathrm{V})$ recorded by EFM at $V_{\mathrm{gate}} = V_{\mathrm{D}}$, V_{SD} marked. (k)−(m) $\widehat{E}_x^{\mathrm{meas}}(x,y)$ maps recorded via EFM of the same area as in h−j, V_{SD} marked, $V_{\mathrm{gate}} = V_{\mathrm{D}}$, $z_{\mathrm{tip}} = 30\,\mathrm{nm}$, $f_{\mathrm{drive}} = 62.34\,\mathrm{kHz}$, sequence of $V_{\mathrm{CPD}}(x,y)$ images (V_{SD} (waiting time/recording time)): 0 V (2 hours/21') → 0.1 V (5'/21') → 0.2 V (5'/21') → 0.1 V (5'/21') → 0 V (5'/21'). The last image serves as reference. (n)−(s) $\widehat{E}_x^{\mathrm{meas}}(x,y)$ recorded by KPFM, V_{SD} marked, $V_{\mathrm{gate}} = V_{\mathrm{D}}$, $z_{\mathrm{tip}} = 30$ nm, $V_{\mathrm{ac}} = 1.1$ V, $f_{\mathrm{drive}} = 62.34$ kHz, sequence of $V_{\mathrm{CPD}}(x,y)$ images (V_{SD} (waiting time/recording time)): -1 V (2 hours/20') → -0.5 V (35'/20') → -0.25 V (10'/20') → 0 V (5'/20') → 0.25 V (5'/20') → 0.5 V (10'/20') → 1 V (35'/20').

Fig. 5n−s demonstrate how areas of inverted $\widehat{E}_x^{\mathrm{meas}}(x, y)$ develop with applied V_{SD}. We generally observe that they weaken with increasing $|V_{\mathrm{SD}}|$ without a clear understanding yet.

In conclusion, we have discovered areas of inverted electric field with respect to the applied source-drain voltage in graphene field-effect transistors at room temperature and moderate mobility. Via carefully analyzing artifacts of the measurement such as SDILD, we could attribute several of these features to local viscous electron flow, in particular, by correlating its appearance with strongly dominating electron-electron scattering compared to electron-disorder scattering. This establishes viscous electron flow as relevant for material parameters used for applications and provides a new method to study these intriguing electron transport phenomena with high spatial resolution.

Supplementary Information

Sample Preparation and Transport Characterization

The field effect graphene devices were made from commercially obtained CVD graphene grown on copper (Graphenia SE) that has been transferred to a SiN (150 nm)/Si(100) substrate after wet chemical etching of copper with $FeCl_3$, using PMMA as a supporting layer for the transfer.[59] The source and drain electrodes of each device are connected to the graphene at the edges according to a procedure described elsewhere.[46] The contacts are defined by a polymer resist AZ5214E via optical lithography followed by removal of graphene from the exposed areas by oxygen plasma in a reactive ion etching chamber operated at 100 W for 30 mins. The contact metals are deposited directly afterwards in order to contact the open bonds of graphene. Firstly, 12 nm Ni is sputtered, which facilitates edge contact with low contact resistance. Then, 50 nm Al is deposited via e-beam evaporation followed by lift-off of the resist. Subsequently, optical lithography is used to remove undesired graphene areas by etching in oxygen plasma. Contact resistances obtained by this process are $100 - 200\,\Omega$ slightly depending on the graphene doping.[46]

Figure S1a shows an optical image of a typical device with the AFM cantilever on top. The device design ensures minimum exposure of the cantilever body to the Si/SiN substrate and, hence, to the electric fields of the gate voltage V_{gate}. Only 2.7 % of the cantilever are in line of sight of the gate dielectric SiN as barely changing during scanning. Hence, gate voltages as high as $\pm 100\,V$ can be applied, while requiring less than 3 V of compensation voltage in KPFM mode as enabled by the Bruker instrument. Furthermore, to reduce the influences of the source and drain voltages, we restrict the measurements to graphene areas away from source and drain as marked, e.g., by the central red rectangle in Fig.S1b.

Four devices from a single chip are probed by KPFM/EFM, each for about one week and, at least, twice. Since the measurements were performed at ambient conditions, the two terminal resistance $R_{\mathrm{transport}}$ of the devices varied continuously with time concerning

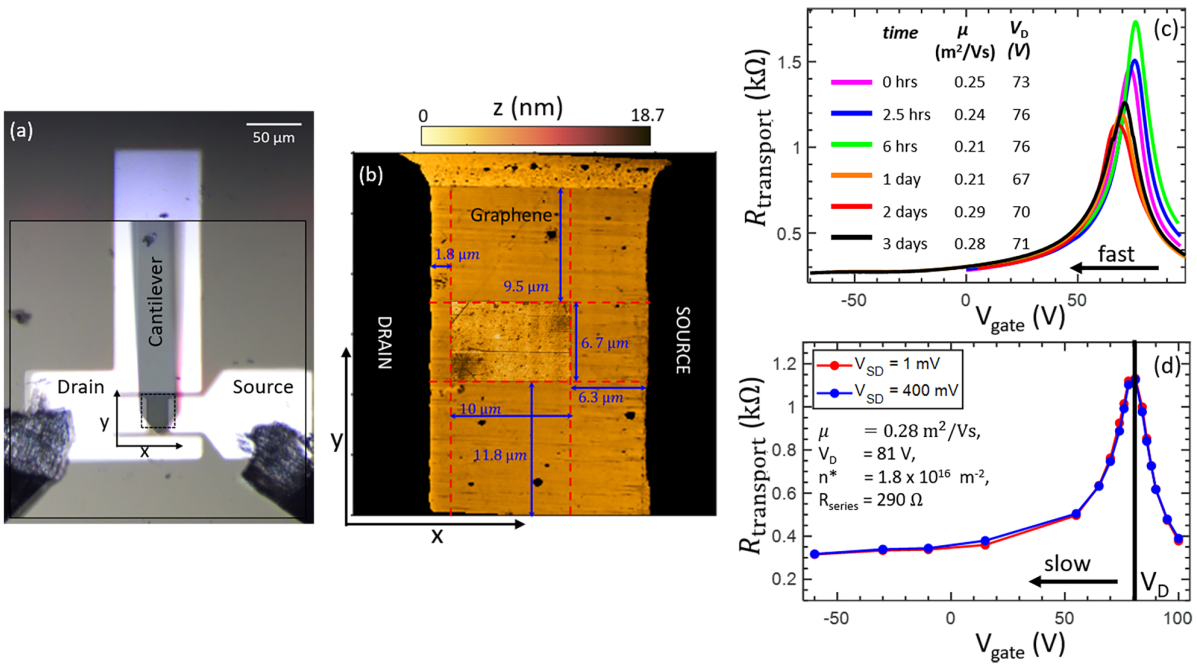

Figure S1: **Experimental Setup.** (a) Optical image of the device in top view with the cantilever above it. The graphene is the darker region below the cantilever. The dashed rectangle marks the area of b. The x and y coordinates depict the scan directions. (b) Topography of the area marked in a as recorded by tapping mode AFM. The central, red rectangle marks the region analyzed in Fig. S7a–f. It is displayed at increased contrast with respect to the color bar on top that is valid for the rest of the image. (c) Gate dependent two terminal resistance for the device analyzed in Fig. 4, main text. The curves are recorded after the time delays as marked, recording time per curve: 8/40/40/1.5/13/2.8 min (from top (0 hrs) to bottom (3 days)), 0.5 s/measurement point. Mobilities μ and Dirac point voltages V_D are deduced from fits by eq. (S.1) revealing, additionally, the residual doping $n^* = (1.5 \pm 0.3) \times 10^{16}\,\mathrm{m}^{-2}$ and the contact resistance $R_\mathrm{series} = (200 \pm 20)\,\Omega$. The arrow indicates the direction of V_gate sweep for all curves. (d) Two-point resistance of the same device as c, but acquired during imaging the maps of Fig. 4a-f, main text . Two V_SD (blue, red) are applied subsequently at each V_gate, 20 min/measurement point. The arrow marks the direction of V_gate sweep. Parameters μ, V_D, n^*, and R_series result from a fit by eq. (S.1).

the voltage at charge neutrality V_{D} and the mobility μ. Moreover, a gate voltage hysteresis appeared, where the sweeps in the reverse direction have been found to be more reproducible. A series of such sweeps are shown for one device in Fig. S1c. Consequently, the reverse sweep direction was exclusively used for all measurements emplyoing sweep speeds not exceeding 0.1 V/s. Moreover, we took care that V_{SD} was changed in the same direction prior to recording images that are compared directly. In addition, a waiting time was established after setting V_{gate} and V_{SD} for each EFM/KPFM image as given in the respective figure captions. Finally, the two-point resistance was continuously monitored during imaging revealing minor variations as depicted in Fig. 1e, main text. Figure S1d shows $R_{\mathrm{transport}}(V_{\mathrm{gate}})$ as measured during an image series. It nicely reproduces the fast $R_{\mathrm{transport}}(V_{\mathrm{gate}})$ sweeps of the same device recorded without imaging (Fig. S1c).

The device mobility μ, the gate voltage at charge neutrality V_{D}, the residual doping n^* at charge neutrality, and the contact resistance R_{series} are deduced from fitting the two-terminal $R_{\mathrm{transport}}(V_{\mathrm{gate}})$ with a relation developed for long range Coulomb type disorder[54,60] (constant mobility):

$$R_{\mathrm{transport}} = R_{\mathrm{series}} + \frac{1}{\mu}\frac{L/W}{\sqrt{\left(C_{\mathrm{gate}}(V_{\mathrm{gate}} - V_{\mathrm{D}})\right)^2 + (n^* e)^2}} \tag{S.1}$$

using the length $L = 18.5\,\mu$m and the width $W = 28\,\mu$m of the graphene area. The gate capacitance per unit area reads $C_{\mathrm{gate}} = \kappa_{\mathrm{SiN}}\epsilon_0/t$ with $\kappa_{\mathrm{SiN}} = 7.5$ and $t = 150\,$nm as dielectric constant and thickness of the dielectric, respectively, and ϵ_0 as the vacuum dielectric constant. The four devices featured $\mu = 2500{-}4000\,\mathrm{cm}^2/\mathrm{Vs}$ and $n^* = (0.8{-}2.7){\times}10^{16}\,\mathrm{m}^{-2}$ with contact resistance $R_{\mathrm{series}} = (160 - 300)\,\Omega$ compatible with previous measurements of identically produced devices.[46]

.

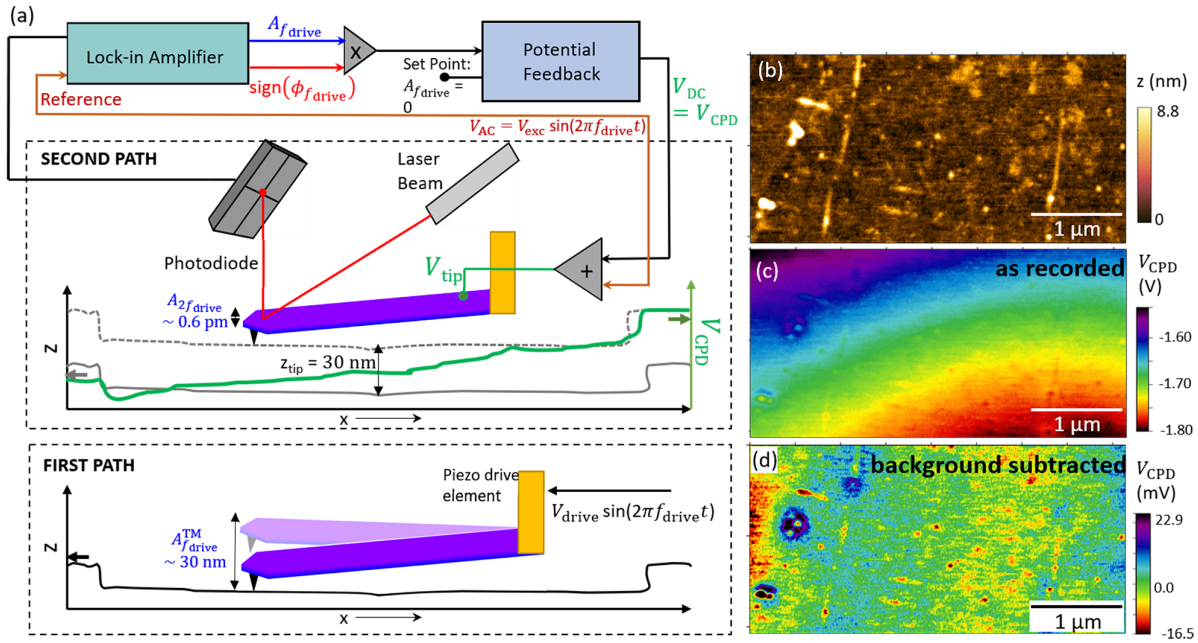

Figure S2: **Kelvin Probe Force Microscopy**. (a) Schematic of amplitude modulation KPFM as implemented in the Dimension Icon AFM setup from Bruker.[61] The lower image shows a profile line $z(x)$ (black) recorded by the cantilever (violet) in tapping mode AFM with amplitude $A^{\mathrm{TM}}_{f\,\mathrm{drive}}$ excited via the voltage $V_{\mathrm{drive}} \sin(2\pi f_{\mathrm{drive}} t)$ applied to the piezo drive of the cantilever. The middle image shows the profile line from the lower image (full grey line) and the same line lifted by z_{tip} (dashed grey line) as traced during recording $V_{\mathrm{CPD}}(x)$ (green line). V_{CPD} is determined at each point by the feedback loop depicted on top. It minimizes the cantilever amplitude $A_{f\,\mathrm{drive}}$ at frequency f_{drive}, while the AC voltage V_{AC} is applied to the tip with constant amplitude V_{exc} simultaneously with a DC voltage V_{DC}, that itself is optimized by the feedback. A remaining amplitude $A_{2f_{\mathrm{drive}}}$ appears at frequency $2f_{\mathrm{drive}}$ (eq. (S.5)). $\phi_{f_{\mathrm{drive}}}$ measures the relative phase between V_{AC} excitation and detected cantilever oscillation. (b) Topography of graphene area for one of the measured devices recorded by tapping mode AFM. (c) Corresponding $V_{\mathrm{CPD}}(x, y)$ map, acquired by KPFM at $V_{\mathrm{gate}} = V_{\mathrm{D}} = 87\,\mathrm{V}$, $V_{\mathrm{SD}} = 0\,\mathrm{V}$. (d) Same map as in c after subtracting a second order polynomial background for horizontal and vertical direction.[62] Image scan parameters: $z_{\mathrm{tip}} = 30$ nm, $A^{\mathrm{TM}}_{f\,\mathrm{drive}} = 30$ nm, $f_{\mathrm{drive}} = 61.355$ kHz, $V_{\mathrm{exc}} = 1.066\,\mathrm{V}$, time/image = 11 min.

Amplitude Modulation KPFM

One of the two scanning probe microscopy methods employed to image the current induced electric fields is Kelvin Probe Force Microscopy with amplitude modulation (AM-KPFM). Figure S2a illustrates its implementation in the Dimension Icon AFM setup from Bruker as used here. It employs a two-path process conducted for each scan line. In the first path, the topography of the sample is acquired by tapping mode AFM. In the second path, called the lift mode, the tip movement mimicks the sample topography at an offset height z_{tip}, while the contact potential difference of the tip with respect to the sample, V_{CPD}, is determined at each point. Hence, the tip retraces the measured topography from the first path with an additional tip-sample distance z_{tip}. During tapping mode, the cantilever oscillation is mechanically driven by a piezo-electric element while the cantilever scans the sample surface employing a z-feedback that regulates the tip-sample distance z to maintain a constant amplitude of the cantilever oscillation $A^{\mathrm{TM}}_{f_{\mathrm{drive}}} \approx 30$ nm. The drive amplitude of the piezoelectric element is $V_{\mathrm{drive}} = 2-3\,\mathrm{V}$ at a drive frequency f_{drive} that is chosen at 50 Hz below the resonance frequency of the free cantilever f_{res} and given in the respective figure captions.

In the second path, both the z-feedback and the piezo drive voltage are switched off, while a potential feedback regulates the DC voltage applied to the cantilever V_{DC}. An AC modulation $V_{\mathrm{AC}}(t) = V_{\mathrm{exc}}\sin(2\pi f_{\mathrm{drive}}t)$ of constant amplitude V_{exc} is superposed to V_{DC} such that the total tip voltage reads $V_{\mathrm{tip}}(t) = V_{\mathrm{DC}}+V_{\mathrm{exc}}\sin(2\pi f_{\mathrm{drive}}t)$. This causes the electrostatic tip-sample interaction force F_{es} to be modulated as[63]

$$F_{\mathrm{es}}(t) = \frac{1}{2}\frac{dC_{\mathrm{ts}}(z)}{dz}(V_{\mathrm{tip}}(t) - V_{\mathrm{CPD}})^2 = F^0_{\mathrm{es}} + (F_{\mathrm{es}})_{f_{\mathrm{drive}}}(t) + (F_{\mathrm{es}})_{2f_{\mathrm{drive}}}(t) \tag{S.2}$$

where $C_{\mathrm{ts}}(z)$ is the distance dependent tip-sample capacitance and

$$F_{\mathrm{es}}^{0} = \frac{1}{2}\frac{dC_{\mathrm{ts}}}{dz}\left[(V_{\mathrm{DC}} - V_{\mathrm{CPD}})^2 + \frac{V_{\mathrm{exc}}^2}{2}\right] \tag{S.3}$$

$$(F_{\mathrm{es}})_{f_{\mathrm{drive}}}(t) = \frac{dC_{\mathrm{ts}}}{dz}(V_{\mathrm{DC}} - V_{\mathrm{CPD}})V_{\mathrm{exc}}\sin(2\pi f_{\mathrm{drive}}t) \tag{S.4}$$

$$(F_{\mathrm{es}})_{2f_{\mathrm{drive}}}(t) = \frac{1}{4}\frac{dC_{\mathrm{ts}}}{dz}V_{\mathrm{exc}}^2\cos(4\pi f_{\mathrm{drive}}t) \tag{S.5}$$

It can be shown that the oscillating $F_{\mathrm{es}}(t)$ causes the cantilever to vibrate with $z_{f_{\mathrm{drive}}}(t) \propto Q \cdot (F_{\mathrm{es}})_{f_{\mathrm{drive}}}(t)/k$ at excitation frequency f_{drive}, if f_{drive} is close to f_{res}.[63] An additional oscillation $z_{2f_{\mathrm{drive}}}(t) \propto (F_{\mathrm{es}})_{2f_{\mathrm{drive}}}(t)/k$ appears at frequency $2f_{\mathrm{drive}}$. Here, $k \approx 3$ N/m is the stiffness constant of the cantilever and $Q \approx 250$ its quality factor (SCM-PIT-V2, Bruker[64]). The amplitude and phase lag of the cantilever oscillation with respect to $V_{\mathrm{AC}}(t)$ is detected by a lock-in amplifier and passed to the potential feedback that nullifies $z_{f_{\mathrm{drive}}}(t)$ by adjusting V_{DC}. Using V_{CPD} as the adjusted V_{DC} as recorded at each position (x, y), a map $V_{\mathrm{CPD}}(x, y)$ results as displayed in Fig. S2c.

Since $z_{f_{\mathrm{drive}}}(t)$ is rendered zero by the feedback, the cantilever oscillates only with $z_{2f_{\mathrm{drive}}}(t)$. The amplitude can be estimated by eq. S.5 using $V_{\mathrm{exc}} = 1.066\,\mathrm{V}$, tip-sample distance $d = A_{f_{\mathrm{drive}}}^{\mathrm{TM}} + z_{\mathrm{tip}} = 60\,\mathrm{nm}$ and assuming the simple model of a charged sphere above an infinite metal surface for the tip-sample capacitance leading to[65] $\frac{dC_{\mathrm{ts}}}{dz} = 2\pi\epsilon_0\frac{R^2}{d(d+R)}$ with tip radius $R = 25\,\mathrm{nm}$. One obtains an amplitude $A_{2f_{\mathrm{drive}}} \approx 0.6\,\mathrm{pm} \ll d$.

Cantilever Contribution

The above description is simplified by assuming a homogeneous surface potential and by neglecting the influence of the electrostatic interaction of the cantilever body with the device. Both are relevant due to the long range nature of electrostatic forces. More precisely, the recorded $V_{\mathrm{CPD}}(x, y)$ is described at each point (x, y) by a convolution of the surface potential map with a point spread function (PSF) deduced from the tip geometry at distance z_{tip}.[40,66] Since AM-KPFM nullifies the f_{drive} component of the tip sample force F_{es} (eq. (2)) and not

the force gradient dF_{es}/dz as EFM (section), the cantilever body as well as tip areas more distant from the apex influence the measured V_{CPD}.[40] This impact is known to reduce the signal intensity, but barely the spatial resolution.[40] For the cantilever of our measurements (SCM-PIT-V2) and $z_{\mathrm{tip}} = 30\,\mathrm{nm}$, the approximate PSF, as given for this cantilever type by Xu *et al.*,[40] reveals a spatial resolution of 60 nm and a reduction of signal intensity by 20 % assuming a homogeneous surface potential.

This is compatible with our results (Fig. S3). The relative drop of transport potential across the graphene as measured by AM-KPFM is only $\sim 80\,\%$ of the applied V_{SD}, but it is 100 % using EFM (Fig. S3b) as expected (section)).[40] The relation for KPFM turns out to be independent on the applied V_{SD} (Fig. S3a) and V_{gate} (Fig. S3b), but changes with z_{tip} (Fig. S3b) as predicted via its PSF.[40] Note that the potential drop across graphene was determined $3\,\mu\mathrm{m}$ away from the lateral metal-graphene interface avoiding influences of the potential inhomogeneities there. Hence, our results confirm the considerations by PSF[40] implying a residual long range influence.

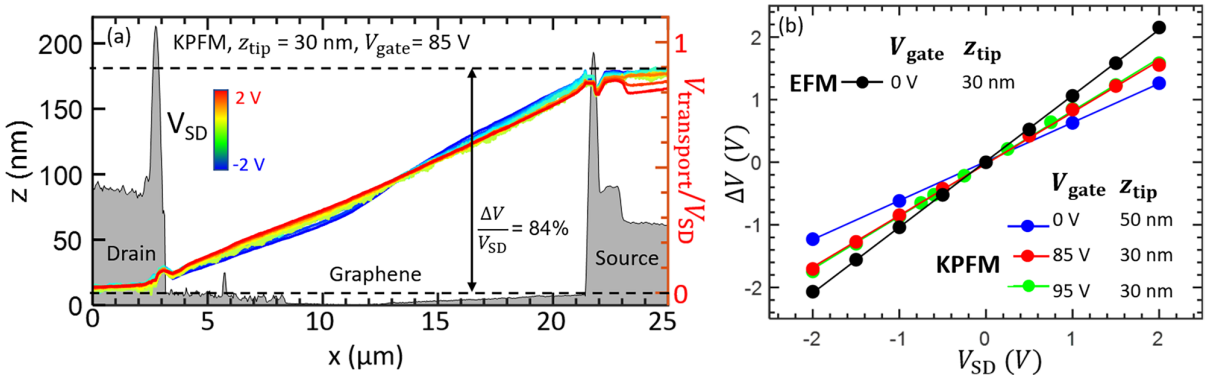

Figure S3: **Transport Potential Drop in KPFM.** (a) Transport potential drops across graphene (colored lines), each averaged from 50 distinct profile lines at the same V_{SD} and normalised by V_{SD} (right vertical scale). Various V_{SD} differing by 0.5 V are color coded, $z_{\mathrm{tip}} = 30\,\mathrm{nm}$, $V_{\mathrm{gate}} = 85\,\mathrm{V}$, $\Delta V := V_{\mathrm{transport}}(x = 25\,\mu\mathrm{m}) - V_{\mathrm{transport}}(x = 0\,\mathrm{nm})$. A topography profile probed by tapping mode AFM is added in grey (left vertical scale). (b) $\Delta V(V_{\mathrm{SD}})$ for different V_{gate}, z_{tip} as marked (slopes: blue: 0.62, red: 0.84, green: 0.82, black: 1.0). For the EFM data, ΔV is deduced from shifts of the maxima of the EFM parabolas measured on the source ($x = 41\,\mu\mathrm{m}$) while the drain is grounded (section).

Background Subtraction

Figure S2c shows a KPFM map of a graphene area recorded at V_{SD} =0 V and V_{gate} =87 V, i.e., at charge neutrality. The displayed area is, at least, 3 μm away from the electrodes and from exposed SiN areas. Thus, residual backgrounds cannot result from the tip apex rendering them long range. Indeed, a dominating, long range contrast developing from the lower right to the upper left appears. It is likely caused by remaining interactions of the cantilever body with exposed SiN areas. Such long-range background is only found in AM-KPFM maps but not in EFM maps corroborating that it is not caused by the tip apex. The increase of $V_{\mathrm{CPD}}(x, y)$ towards the upper left meets the expectation from the geometry of the exposed SiN areas (Fig. S1a) and the positive V_{gate}. Due to the inclination of 10° of the cantilever towards the tip, the distance of the cantilever body part above SiN decreases relative to the SiN by moving the cantilever into this direction and, hence, the interaction force to the SiN increases.

To get rid of the long-range background, we apply a 2$^{\mathrm{nd}}$ order polynomial background subtraction using Gwyddion.[62] The resulting map after subtraction is displayed in Fig. S2d featuring an obvious correlation with the simultaneously recorded topography (Fig. S2b), e.g., at the two nearly vertically propagating wrinkles or at the two large bumps on the left that obviously change the local doping. This justifies the subtraction method featuring a spatial resolution of about 20 nm and a V_{CPD} resolution of about 10 mV.

Of course, the background subtraction also removes the spatial average of V_{CPD} and the linear potential drop induced by V_{SD}. They are, however, required for the doping maps and the electric field maps, respectively. For the electric field maps, we do not apply the background subtraction, but rely on the subtraction of two $V_{\mathrm{CPD}}(x, y)$ maps recorded at the same V_{gate} (eq. (S.10)) and, hence, removing the background, that is dominated by the gate voltage that penetrates to the cantilever, automatically. For the doping maps (eq. (S.13)), we add to the background subtracted $V_{\mathrm{CPD}}(x, y)$ an averaged value $\overline{V}_{\mathrm{CPD}}$ as deduced from a straightforward capacitive charging model of the graphene by V_{gate} (section

). This procedure is corroborated by the excellent agreement between the simulated electric field maps (Fig. 2f,h, main text) as directly deduced from doping maps (section) with the experimentally measured electric field maps (Fig. 2g,i, main text).

Noise and Sensitivity

Two major sources of noise are known for KPFM.[67] Firstly, thermal fluctuations of the cantilever oscillation are present due to Brownian motion. Secondly, sensor noise from detecting the optical beam deflection (OBD) contributes. Using established formulas,[67] we find the thermal noise to be $n_{\text{thermal}} = 1.9\,\text{pm}/\sqrt{\text{Hz}}$ using our parameters $Q = 250$, $f_{\text{res}} = 62.34\,\text{kHz}$ and $T = 300\,\text{K}$. A typical value for the OBD sensor noise is $n_{\text{OBD}} = 100\,\text{fm}/\sqrt{\text{Hz}}$,[67] i.e., negligible. For the typical bandwidth of the feedback loop $B \approx 5\,\text{Hz}$, we get an amplitude noise at f_{drive} of $n_{\text{thermal/OBD}}\sqrt{B} \approx 4\,\text{pm}$. This imposes a lower limit on the V_{CPD} precision. At $z_{\text{tip}} = 30\,\text{nm}$ and AC voltage amplitude $V_{\text{AC}} = 1.066\,\text{V}$, we find this limit to be $\delta V_{\text{CPD}} = 10\,\text{mV}$.[67] This is roughly consistent with the noise in $V_{\text{CPD}}(x, y)$ maps, e.g., in Fig. S2d, i.e., we find RMS fluctuations within areas of $0.5\,\mu\text{m} \times 0.5\,\mu\text{m}$ of 5–20 mV. It also roughly agrees with the data sheet from Bruker promising a noise level of $\sim 10\,\text{mV}$ and with other experiments in the literature.[47,63,68]

Electrostatic Force Microscopy

As second method, we employed Electrostatic Force Microscopy (EFM), well established to map surface potentials with high resolution.[44,69] Like KPFM (section), it uses a two step process acquiring the topography in a first path. After lifting the tip for the second path, contrary to KPFM, the cantilever is oscillated by an AC voltage applied to a piezoelectric element, while a DC voltage V_{tip} is applied to the tip (Fig. S4a). This V_{tip} induces an attractive electrostatic force between tip and sample via image charges in the sample (eq. (S.2)) that causes a decrease in resonance frequency of the cantilever f_0 with resulting

shift of the phase vs. frequency curve $\phi_{\mathrm{EFM}}(f)$ (Fig. S4e). Probing at the excitation frequency $f_{\mathrm{drive}} < f_0$, the electrostatic force changes the phase lag between cantilever oscillation and voltage oscillation at the piezo (Fig. S4e) as well as the amplitude of the cantilever oscillation A_{EFM}. The measured A_{EFM} and ϕ_{EFM} are both related to the electrostatic tip-sample force gradient that must be nullified to detect the local V_{CPD}. Note that ϕ_{EFM} depicts the phase lag of the exciting oscillation with respect to the cantilever oscillation after being nullified prior to each measurement at the resonance frequency of the free cantilever oscillation.

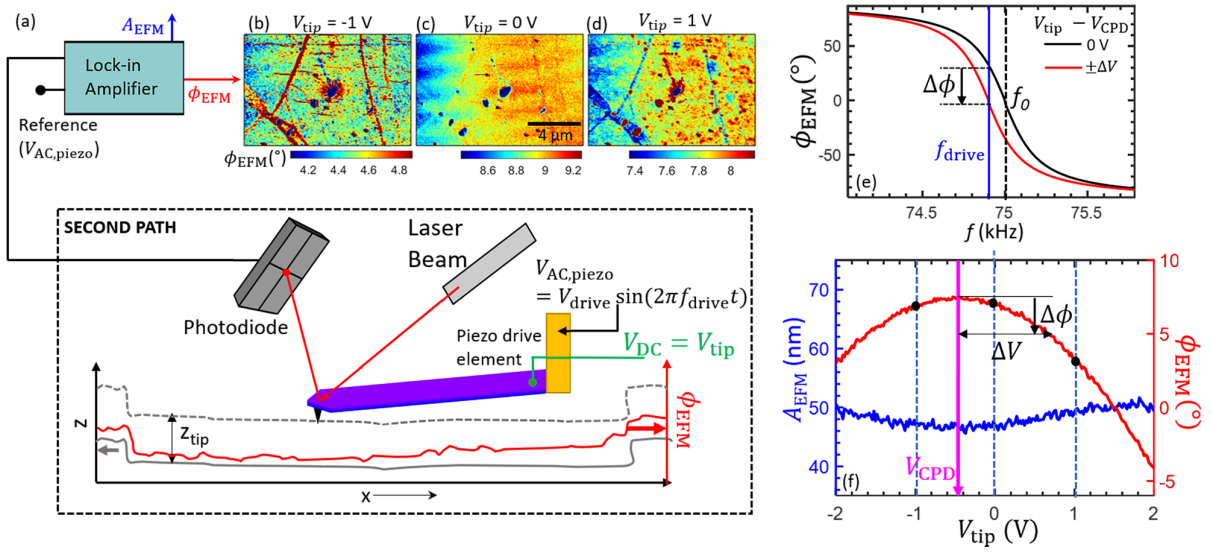

Figure S4: **Electrostatic Force Microscopy**. (a) Sketch of the cantilever (violet) during the second path (lift mode) including the detection scheme (laser, photodiode). Full grey line: Topography $z(x)$ recorded during the first path. Dashed grey line: Topography line after lifting the cantilever by z_{tip} as tracked during the second path. Red line: phase of cantilever oscillation $\phi_{\mathrm{EFM}}(x)$ as recorded during the second path. The cantilever is continuously excited by $V_{\mathrm{AC,piezo}}$, applied to the piezo element at frequency f_{drive} slightly below the resonance frequency of the free cantilever f_{res}. A DC tip voltage V_{tip} changes the amplitude A_{EFM} and phase ϕ_{EFM} of the cantilever oscillation at f_{drive} as recorded by lock-in amplifier. (b–d) Three exemplary $\phi_{\mathrm{EFM}}(x, y)$ maps of *one* graphene area (topography in Fig. 5h, main text) recorded at three different V_{tip} as marked. (e) Simulation of $\phi_{\mathrm{EFM}}(f)$ for two distinct $V_{\mathrm{tip}} - V_{\mathrm{CPD}}$, $f_0 = 75\,\mathrm{kHz}$, $Q = 240$ as present for the used SCM-PIT-V2 cantilever. The downward arrow marks the decrease in ϕ_{EFM} at f_{drive} due to the electrostatic force induced by V_{tip}. (f) Measured A_{EFM} (blue, left axis) and ϕ_{EFM} (red, right axis) as function of V_{tip} for a centrally located point on graphene, $V_{\mathrm{gate}} = 65\,\mathrm{V}$, $V_{\mathrm{SD}} = 0\,\mathrm{V}$. V_{CPD} marks the voltage at the ϕ_{EFM} maximum. $\Delta\Phi$ marks the phase shift with respect to V_{CPD} induced by $V_{\mathrm{tip}} = 0.8\,\mathrm{V}$. The vertical dashed lines with black dots indicate the three V_{tip} as used for recording $\phi_{\mathrm{EFM}}(x, y)$ maps and subsequently deducing $V_{\mathrm{CPD}}(x, y)$ maps.

Assuming the cantilever as a damped, driven harmonic oscillator disturbed by a force that is small compared to the restoring force of the cantilever and that varies slowly on the scale of the oscillation amplitude, the following expression applies for the induced resonance frequency shift Δf_0[70] (k: cantilever stiffness constant, F_{es}: electrostatic force according to eq. (S.2)).

$$\Delta f_0 = -\frac{f_0}{2k}\,\frac{\partial F_{\mathrm{es}}}{\partial z}. \tag{S.6}$$

For $f_{\mathrm{drive}} \approx f_0$ and $Q \cdot \Delta f_0 / f_0 \ll 1$, the corresponding phase shift reads:[44]

$$\Delta\phi_{\mathrm{EFM}}(f_{\mathrm{drive}}) = -\arcsin\left(\frac{2Q}{f_0}\,\Delta f_0\right) \approx -\frac{Q}{k}\,\frac{\partial F_{\mathrm{es}}}{\partial z}. \tag{S.7}$$

Hence, the change of $\phi_{\mathrm{EFM}}(f_{\mathrm{drive}})$ is proportional to the force gradient. This renders EFM more sensitive to local surface potentials than AM KPFM, itself minimizing the force instead (section). Long range forces acting on the cantilever body contribute much less to EFM via their less steep gradient.[40] Indeed, $\phi_{\mathrm{EFM}}(x, y)$ maps are found devoid from any significant long range background (Fig. S4b–d, Fig. S5a). The spatial resolution of EFM improves with decreasing z_{tip}. For the selected SCM-PIT-V2 cantilever and $z_{\mathrm{tip}} = 20\,\mathrm{nm}$ (Fig. 3, main text), the resolution is approximately $1.1 \cdot z_{\mathrm{tip}} + 11\,\mathrm{nm} = 33\,\mathrm{nm}$.[40]

Substituting F_{es} from eq. (S.2) into eq. (S.7) implies a quadratic dependence of $\Delta\phi_{\mathrm{EFM}}$ on V_{tip} reading

$$\Delta\phi_{\mathrm{EFM}}(x, y) = -\frac{Q(x, y)}{2k}\,\frac{d^2 C_{\mathrm{ts}}(x, y)}{dz^2}\,\left(V_{\mathrm{tip}} - V_{\mathrm{CPD}}(x, y)\right)^2, \tag{S.8}$$

where the quality factor Q and the tip sample capacitance C_{ts} are position dependent as affected by local variations of dissipation and screening, respectively, due to, e.g., adsorbates or doping fluctuations. Nevertheless, the maximum of $\phi_{\mathrm{EFM}}(V_{\mathrm{tip}})$ is a direct measure of V_{CPD}. Indeed, the measured $\phi_{\mathrm{EFM}}(V_{\mathrm{tip}})$ at a single point features a parabola as shown by the fit in Fig. 1b, main text. Minor deviations at larger voltages are most likely caused by

the influence of quantum capacitance that is not captured by eq. (S.2). To determine V_{CPD} for each position (x, y), we probe $\phi_{\mathrm{EFM}}(x, y)$ at only three $V_{\mathrm{tip}} = -1, 0, 1\,\mathrm{V}$ (Fig. S4f) and use the three points for fitting a parabolic function

$$\phi_{\mathrm{EFM}}(x, y) = -\kappa(x, y)\left(V_{\mathrm{tip}} - V_{\mathrm{CPD}}(x, y)\right)^2 + \phi_0(x, y) \tag{S.9}$$

via three parameters, namely the curvature $\kappa(x, y)$ and the maximum at $(\phi_0,\, V_{\mathrm{CPD}})(x, y)$. Hence, we take the local nature of all three parameters into account with $\phi_0(x, y)$ caused by local forces that are not dependant on V_{tip}. We choose the extrema of $V_{\mathrm{tip}} = \pm 1\,\mathrm{V}$ large enough to obtain high precision of the fit, but still small enough to avoid deviations from the parabola due to quantum capacitance.

Noise and Sensitivity

To illustrate the principle, Fig. S5a displays a $V_{\mathrm{CPD}}(x, y)$ map of an electron doped graphene area as obtained by a parabolic fit using eight V_{tip} for each position (x, y) instead of three, hence, enabling better precision. Features are discernable at several graphene folds, wrinkles and point defects (compare with the topography in Fig. 5h, main text). These topographic features obviously exhibit distinct surface potentials. Importantly, no long range background had to be subtracted. Figure S5b shows two selected sets of measured $\phi_{\mathrm{EFM}}(V_{\mathrm{tip}})$ at the eight V_{tip} together with a parabolic fit and a 7^{th} order polynomial fit. The two fits reveal nearly identical maxima.

Figure S5c displays the variation of the curvature of the fitted parabolas with V_{gate} (main) and with position (inset). While the V_{gate} dependence is rather irregular exhibiting fluctuations of about 5 % only, the position dependence exhibits features at folds and wrinkles that likely exhibit different dissipation strengths leading to different local $Q(x, y)$. Variations in Φ_0, related to the forces that do not depend on V_{tip}, are about 0.6° for, both, V_{gate} dependence and position dependence, but without obvious correlations to topographic features

(not shown).

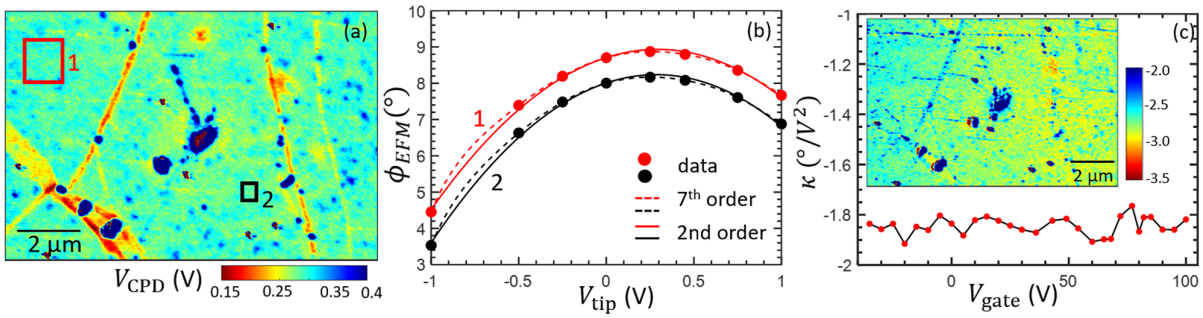

Figure S5: **Parabolic fits of** $\phi_{\mathrm{EFM}}(V_{\mathrm{tip}})$. (a) $V_{\mathrm{CPD}}(x, y)$ map of graphene measured by EFM via parabolic fits of eight recorded $\phi_{\mathrm{EFM}}(V_{\mathrm{tip}})$ values for each location (x, y) (eq. (S.9)), $V_{\mathrm{gate}} = 100\,V$, $V_{\mathrm{SD}} = 0\,V$, $z_{\mathrm{tip}} = 30\,\mathrm{nm}$. The corresponding topography is shown in Fig. 5h, main text. (b) Variation of ϕ_{EFM} with V_{tip} for the two marked regions in (a). The solid/dashed lines are fits to the measured data points with the specified polynomial order. The black curves are shifted downwards for better visibility. (c) Curvature $\kappa(V_{\mathrm{gate}})$ resulting from parabolic fits as in (b) (eq. S.9) and displayed for a single location. Inset: $\kappa(x, y)$ of the same area as in (a), $V_{\mathrm{gate}} = 100\,V$, $V_{\mathrm{SD}} = 0\,V$, $z_{\mathrm{tip}} = 30\,\mathrm{nm}$.

For $V_{\mathrm{CPD}}(x, y)$ mapping by EFM, we recorded only three $\phi_{\mathrm{EFM}}(V_{\mathrm{tip}})$ at each location that are fitted by a parabola (eq. (S.9)). The resulting noise is estimated in the following. Continuous sweeps of $\phi_{\mathrm{EFM}}(V_{\mathrm{tip}})$ consisting of 512 points and recorded at different V_{gate} revealed an average RMS deviation from the parabola of $\delta\phi_{\mathrm{EFM}} = 0.09°$ at a recording time per point of 1.5 ms. The RMS deviation with respect to the parabola dropped continuously, if one employs Gaussian averaging of $\phi_{\mathrm{EFM}}(V_{\mathrm{tip}})$ prior to fitting, as expected. Moreover, fits of higher polynomial order only slightly decreased $\delta\phi_{\mathrm{EFM}}$, e.g., by less than 5% up to a fit order of ten. This corroborates that the parabola is a very good approximation of $\phi_{\mathrm{EFM}}(V_{\mathrm{tip}})$. Since recording times of 3.4 ms are employed for the three $\phi_{\mathrm{EFM}}(V_{\mathrm{tip}})$ used for $V_{\mathrm{CPD}}(x, y)$ maps, the RMS error becomes $\delta\phi_{\mathrm{EFM}} = 0.09° \times \sqrt{1.5/3.4} = 0.06°$. We used this $\delta\phi_{\mathrm{EFM}}$ to deduce the resulting error in V_{CPD} by numerical simulations revealing $\delta V_{\mathrm{CPD}} \approx 2\,\mathrm{mV}$ at $V_{\mathrm{CPD}} \approx 0.2\,\mathrm{V}$ such as in Fig. 3, main text. This largely fits with the uncorrelated noise that we observe in maps experimentally (section).

Electric Fields due to Current Flow

To map the current induced electric fields, we measure the change of the contact potential difference $V_{\mathrm{CPD}}(x, y)$ after applying a source-drain voltage V_{SD}. This is dubbed the transport voltage $V_{\mathrm{transport}}(x, y, V_{\mathrm{SD}})$ defined as.

$$V_{\mathrm{transport}}(x, y, V_{\mathrm{SD}}) = V_{\mathrm{CPD}}(x, y, V_{\mathrm{SD}}) - V_{\mathrm{CPD}}(x, y, V_{\mathrm{SD}} = 0\,V) \tag{S.10}$$

The negative spatial gradient of $V_{\mathrm{transport}}(x, y, V_{\mathrm{SD}})$ is the transport induced electric field reading

$$\mathbf{E}^{\mathrm{meas}}(x, y) = -\nabla V_{\mathrm{transport}}(x, y). \tag{S.11}$$

The derivation implicitly assumes that the static work-function fluctuations of the two subtracted $V_{\mathrm{CPD}}(x, y)$ maps remain unchanged and therefore cancel (section).

Figure S6a shows a $V_{\mathrm{transport}}(x, y)$ map derived from KPFM maps of $V_{\mathrm{CPD}}(x, y)$ according to eq. (S.10) and after normalizing to V_{SD}. The image employs $V_{\mathrm{SD}} = 0.5\,\mathrm{V}$ at charge neutrality. The x and y components of the resulting in-plane electric field $\mathbf{E}^{\mathrm{meas}}(x, y)$ (eq. (S.11)) are displayed in Fig. S6b and c, respectively. Figure S6g shows a vector representation of $\mathbf{E}^{\mathrm{meas}}(x, y)$ represented by arrows on the colored background of the deduced charge carrier density $n(x, y)$ as present at $V_{\mathrm{SD}} = 0.5\,\mathrm{V}$ (eq. (S.14)).

Figure S6d-f and h show the same data, but deduced from the $V_{\mathrm{CPD}}(x, y)$ maps after 2^{nd} order polynomial background subtraction (section). This naturally removes the constant electric field along the applied V_{SD} and, thus, highlights deviations from this average electric field, but it prohibits the direct identification of inverted electric fields. Correlations between doping and electric field get more apparent, e.g., hole (electron) doped regions in this particular area tend to reduce (increase) the electric field in x direction with respect to the average field. Moreover, it gets more easy within the vector maps with background subtraction to identify electric fields pointing in different y directions (Fig. S6g). Finally,

one can identify source like areas (e.g. upper left area) or sink like areas (e.g. upper fold area) of the current induced electric fields.

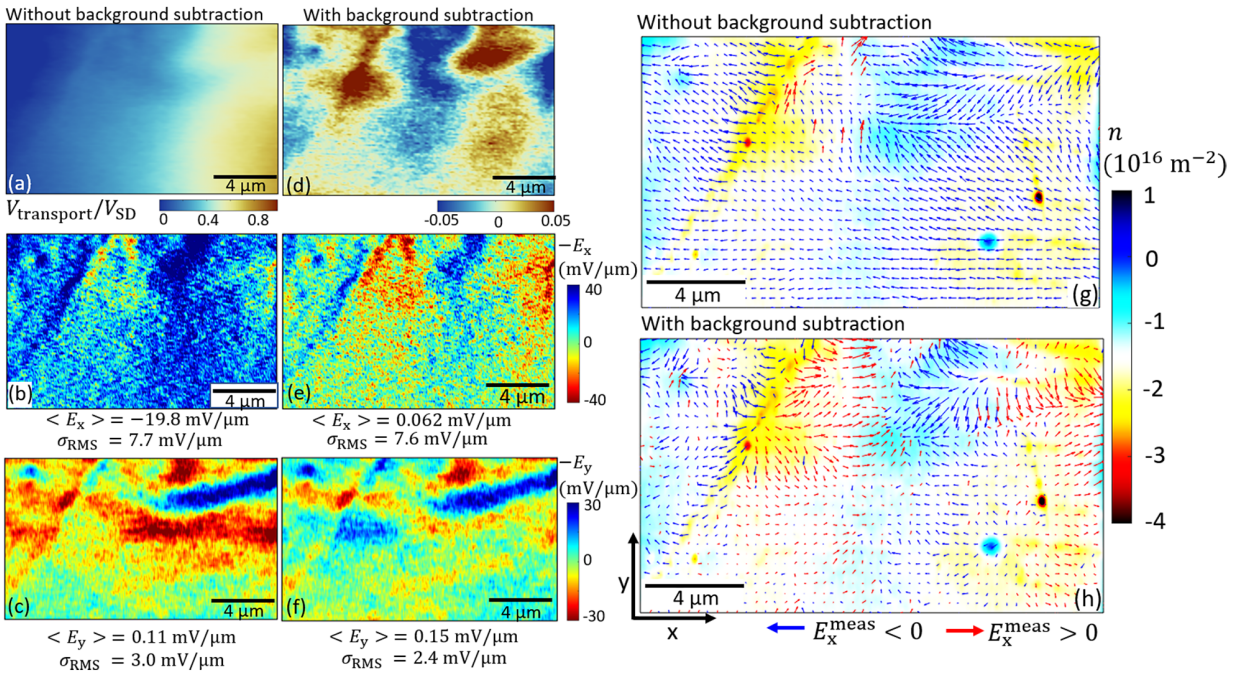

Figure S6: **Current Induced Electric Fields after Background Subtraction.** (a) $V_{\text{transport}}(x, y)/V_{\text{SD}}$ map using KPFM for recording $V_{\text{CPD}}(x, y)$ at $V_{\text{SD}} = 0.5\,\text{V}$ and $V_{\text{SD}} = 0\,\text{V}$ as input for eq. (S.10), $V_{\text{gate}} - V_{\text{D}} = -5\,\text{V}$, corresponding topography: Fig. 1f, main text. (b, c) Maps of x and y component of the electric field, respectively, as deduced by eq. (S.11) using a. Average electric fields $\langle E_{x,y} \rangle$ and the RMS standard deviations σ_{RMS} are marked below the images. The latter is determined within boxes of $(1\,\mu\text{m})^2$ and averaged over all boxes afterwards. (d) Same as a, but after removal of a 2^{nd} order polynomial background from the two constituting $V_{\text{CPD}}(x, y)$ maps (section). (e, f) Maps of x and y component of the electric field derived from d via eq. (S.11). (g) Vector plot of in-plane electric field $\mathbf{E}^{\text{meas}}(x, y)$ deduced via eq. (S.11) from a. The arrows are colored blue (red), if pointing forward (backward) with respect to the applied V_{SD}. The background color shows the doping distribution $n(x, y)$ at $V_{\text{SD}} = 0.5\,\text{V}$ (eq. (S.14)). (h) Same as g, but deduced from d.

Noise Filtering

Performing a nearest neighbor differentiation of $V_{\text{transport}}(x, y)$ to obtain $\mathbf{E}^{\text{meas}}(x, y)$ maps (eq. S.11) revealed uncorrelated noise for both components with strength $\delta E_x^{\text{meas}} \approx \delta E_y^{\text{meas}} \approx 100\,\text{mV}/\mu\text{m}$ (Fig.S7a). This uncorrelated noise obscured the observation of any feature. This is likely of electric origin at the piezoelectric actuators reducing the accuracy to determine

V_{CPD} in EFM (section).

To reduce the overwhelming noise, we employ two filtering processes. On one hand, we apply a spatial Gaussian averaging with full width at half maximum Γ to $V_{\mathrm{transport}}(x, y)$ maps. On the other hand, we use locations that are further apart from each other for the differentiation, i.e.,

$$E_x^{\mathrm{meas}}(x, y) = \frac{V_{\mathrm{transport}}(x, y) - V_{\mathrm{transport}}(x - \Delta x, y)}{\Delta x}$$
$$E_y^{\mathrm{meas}}(x, y) = \frac{V_{\mathrm{transport}}(x, y) - V_{\mathrm{transport}}(x, y - \Delta y)}{\Delta y} \tag{S.12}$$

with Δx and Δy being the chosen distances in the respective directions. The RMS fluctuations $\delta E_x^{\mathrm{meas}}$ and $\delta E_y^{\mathrm{meas}}$ scale with $1/\Delta x$ and $1/\Delta y$, respectively, according to error propagation. This naturally improves the signal to noise ratio at the expense of spatial resolution.

This second approach is visualized for an experimentally measured $V_{\mathrm{transport}}(x, y)$ map in Fig. S7a–c. Stable structures appear at $\Delta x \geq 0.91\,\mu$m, i.e., using a distance of 35 measurement points for Δx. The remaining uncorrelated noise exhibits a standard variation $\sigma_{E_x} = 5\,\mathrm{mV}/\mu\mathrm{m}$ as deduced by analyzing multiple boxes of $(0.3\,\mu\mathrm{m})^2$, much smaller than the apparent features sizes. This can be compared with the error $\delta V_{\mathrm{CPD}} = 2\,\mathrm{mV}$ resulting from the $\Phi_{\mathrm{EFM}}(V_{\mathrm{tip}})$ noise (section). Error propagation implies $\delta V_{\mathrm{transport}} = 3\,\mathrm{mV}$ (eq. (S.10)) and, respectively, $\delta E_x^{\mathrm{meas}} = 5\,\mathrm{mV}/\mu\mathrm{m}$ for $\Delta x = 0.91\,\mu$m (eq. S.12) in very good agreement with the measured noise of $5\,\mathrm{mV}/\mu\mathrm{m}$.

Figure S7g shows the same procedure of filtering via large Δx for a fictitious electric field $E_x(x)$ featuring a dipolar structure (black line) that is mixed with uncorrelated noise in $V_{\mathrm{transport}}(x)$ of strength $\delta V_{\mathrm{transport}} = 16\,\mathrm{mV}$ prior to using different Δx to determine $E_x^{\mathrm{meas}}(x)$ according to eq. (S.12) (colored lines). Obviously, the feature width and height are barely changed by the Δx filtering, but the dipolar feature is slightly shifted to the right. In

contrast, the Gaussian averaging makes the features wider and weaker in amplitude, while maintaining its center position (Fig. S7h). This is also visible in the accordingly Gaussian filtered experimental images (Fig. S7d-f).

Since our main interest is the feature size and the feature strength, in particular, during the analysis of Fig. 3, main text, we optimize Δx (eq. S.12) towards the lowest possible signal/noise ratio, where features get significantly stronger than the noise floor, but use only a mild Gaussian averaging with $\Gamma \leq 100\,\mathrm{nm}$. Table S1 summarizes the chosen Δx and Γ for all electric field maps presented in main text and supplement.

Eventually, Fig. S7i and j show the rms electric field noise $\sigma_{E_x}(\Delta x)$, determined within multiple boxes of size $(0.3\,\mu\mathrm{m})^2$ (average of all boxes within one image) for different V_{gate} and V_{SD}, respectively. The fitted slope in the double-logarithmic plots (lines) consistently reveals $\sigma_{E_x} \propto \Delta x^{-1}$, as expected from the discussion above. This evidences uncorrelated $E_x^{\mathrm{meas}}(x, y)$ noise. In line, the correlation length of $E_x^{\mathrm{meas}}(x, y)$ at smallest possible $\Delta x = 26\,\mathrm{nm}$ (eq. S.12) is $\xi \approx 30\,\mathrm{nm}$ only, i.e., the image resolution. Note that the noise depends barely on V_{SD} and V_{gate}.

Table S1: Table: Filter parameters for all electric field maps of main text and supplement.

Figure	Method	Γ	Δx	Δy
1d	KPFM	92 nm	1.17 μm	0.12 μm
1g	KPFM	81 nm	0.43 μm	0.12 μm
2f-i	KPFM	93 nm	0.39 μm	0.08 μm
3c–d,	EFM	86 nm	0.47 μm	0.03 μm
3e–f, S8m–n,	EFM	62 nm	0.91 μm	0.03 μm
4	KPFM	31 nm	0.39 μm	0.05 μm
5a–f, S6b–c, S14	KPFM	61 nm	0.52 μm	0.12 μm
5g	KPFM	61 nm	0.52 μm	0.58 μm
5i–m	EFM	77 nm	0.39 μm	0.04 μm
5n–s	KPFM	77 nm	0.82 μm	0.05 μm
S6e–f	KPFM	81 nm	0.52 μm	0.93 μm
S6g–h	KPFM	61 nm	0.52 μm	0.93 μm
S10c	KPFM	77 nm	0.33 μm	0.05 μm
S10d	KPFM	99 nm	0.03 μm	0.05 μm

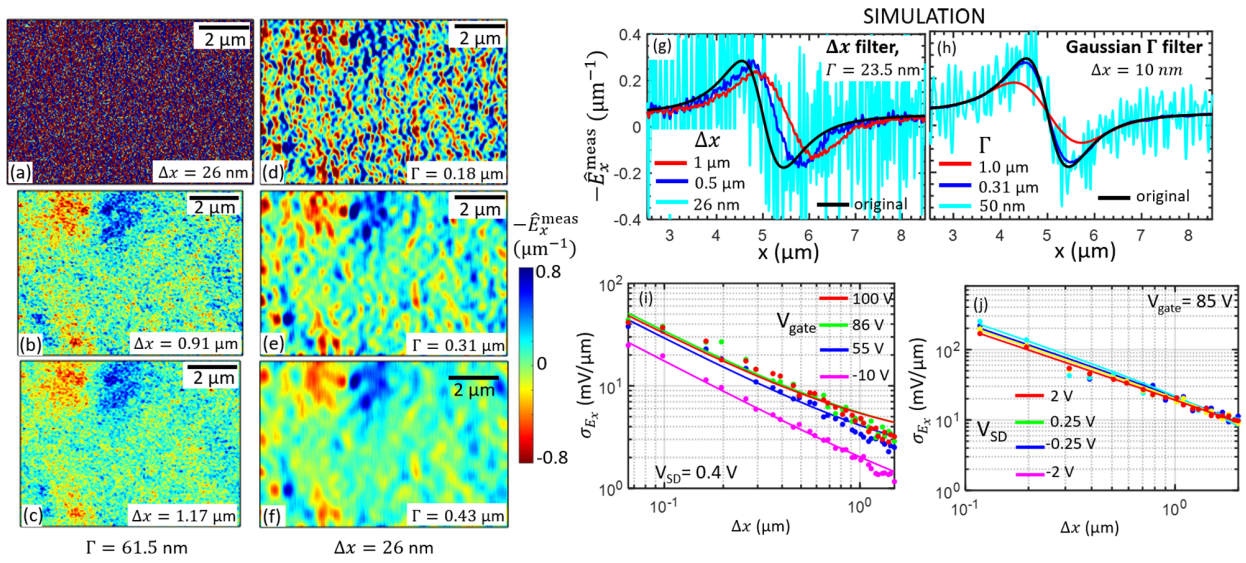

Figure S7: **Filtering procedure for electric field maps.** (a–c) Experimentally measured $\widehat{E}_x^{\mathrm{meas}}(x,y)$ (EFM) using eq. (S.12) with different values of Δx as indicated after mild Gaussian averaging of $V_{\mathrm{transport}}(x,y)$ with $\Gamma = 61.5\,\mathrm{nm}$, the upper left area of b corresponds to Fig. 3e, main text. (d–f) $\widehat{E}_x^{\mathrm{meas}}(x,y)$ using the same $V_{\mathrm{transport}}(x,y)$ map as in a–c, but using Gaussian averaging with different Γ before employing $\Delta x = 26\,\mathrm{nm}$ for differentiation (eq. (S.12)). (g) Simulated dipolar feature of $\widehat{E}_x(x)$ (black line) and the same feature after superposition with white noise of strength $\delta V_{\mathrm{transport}} = 16\,\mathrm{mV}$ in the constituting $V_{\mathrm{transport}}(x)$ at $V_{\mathrm{SD}} = 0.1\,\mathrm{V}$ and subsequent application of eq. (S.12) with the indicated Δx (colored lines). (h) Same as g concerning simulated dipole (black line) and noise superposition, but using subsequently Gaussian averaging with different Γ as marked (colored lines). (i,j) RMS noise of experimental $E_x^{\mathrm{meas}}(x,y)$ maps, $\sigma_{E_x}(\Delta x)$, for different V_{gate} (i) and V_{SD} (j) (KPFM). The noise for each Δx is deduced within boxes of $0.3\,\mu\mathrm{m} \times 0.3\,\mu\mathrm{m}$ covering the whole image. Subsequently, the noise of all boxes is averaged. The solid lines are linear fits revealing $\sigma_{E_x} \propto \Delta x^{-1}$.

Temporal Stability of Dopant Distribution

The transport potential $V_{\mathrm{transport}}(x, y)$ according to eq. (S.10) quantifies the potential drop due to charge flow, if the work-function fluctuations in the measured region remain the same while acquiring the two $V_{\mathrm{CPD}}(x, y)$ maps, biased and unbiased. However, the ambient conditions during recording partially lead to local charging and discharging depending on the history of V_{gate} and V_{SD}. An example is shown in Fig. S8a–c, where changes in $V_{\mathrm{CPD}}(x, y)$ appear, albeit the maps are recorded subsequently without changing V_{gate} or V_{SD} and a full day after setting these voltages. However, changes after recording Fig. S8c are much less pronounced (Fig. S8d–f), albeit V_{SD} was cycled in between indicating that a first imaging itself leads to equilibration of the doping pattern.

Hence, it is crucial to reduce the uncontrolled charging processes. Therefore, we firstly monitored the two-terminal $R_{\mathrm{transport}}$ continuously. It changed minimally after ramping V_{gate} to about 100 V and then ramp it down slowly by $\sim 0.1\,V/s$ until the device resistance is maximized signalling charge neutrality. Figure S8g shows a time trace of $R_{\mathrm{transport}}$ after such stabilization revealing only small fluctuations of about 5 % after a waiting time of roughly 5 hours. Using this procedure, stability at the local scale has still to be ensured. This was more involved and not always successful. There is no direct way to experimentally map the doping distribution, while applying a finite V_{SD}. Hence, we checked the doping distribution by recording $V_{\mathrm{CPD}}(x, y, V_{\mathrm{SD}} = 0\,\mathrm{V})$ maps before and after recording $V_{\mathrm{CPD}}(x, y, V_{\mathrm{SD}} \neq 0\,\mathrm{V})$ maps. Figure S8h–n display characteristic features of a successful image sequence, namely a minimum change in $V_{\mathrm{transport}}$ while cycling V_{SD} and very similar spatially averaged V_{CPD} values for images recorded at the same V_{SD} but after a distinct V_{SD} history (Fig. S8h). Obviously, the first two images exhibit a rather different $\langle V_{\mathrm{CPD}}(x, y)\rangle$ in line with the changes in Fig. S8a–c, implying again that the first maps within a certain area change the lateral doping distribution more strongly, likely via the applied tip voltages. However, stable subsequent images can be often recorded afterwards. Consequently, the $V_{\mathrm{transport}}(x, y)$ maps deduced from a stable sequence are nearly identical, if distinct reference images recorded at

$V_{\mathrm{SD}} = 0\,\mathrm{V}$ are employed (eq. (S.10)). This is visible by comparing Fig. S8i and k as well as Fig. S8j and l, that used image 6 and image 10 as reference, respectively. The similarity naturally also applies for the resulting electric field maps in Fig. S8m–n. These kind of images, selected by adequate monitoring, are, hence, reliably attributed to consequences of the applied V_{SD} (discussion of Fig. 3, main text).

Doping Distribution from $V_{\mathrm{CPD}}(x, y)$ Maps

Spatial fluctuations of the contact potential difference between tip and graphene are related to doping fluctuations of the graphene.[48] The corresponding doping density $n_0(x, y)$ can be deduced via $|e|\,(V_{\mathrm{CPD}}(x, y) - V^0_{\mathrm{CPD}}) = E_{\mathrm{F}} - E_{\mathrm{D}}(x, y)$, where $E_{\mathrm{F}} := 0\,\mathrm{eV}$ is the Fermi energy of graphene, $E_{\mathrm{D}}(x, y)$ is the local Dirac point energy, and V^0_{CPD} is the contact potential difference between the tip and charge neutral graphene. The resulting doping distribution $n_0(x, y)$ at $V_{\mathrm{SD}} = 0\,\mathrm{V}$ reads

$$n_0(x, y) = \frac{e^2}{\pi}\,\mathrm{sign}\big[V_{\mathrm{CPD}}(x, y, V_{\mathrm{SD}} = 0\,\mathrm{V}) - V^0_{\mathrm{CPD}}\big]\,\left(\frac{V_{\mathrm{CPD}}(x, y, V_{\mathrm{SD}} = 0\,\mathrm{V}) - V^0_{\mathrm{CPD}}}{\hbar v_{\mathrm{F}}}\right)^2, \tag{S.13}$$

whith the Fermi velocity of graphene $v_{\mathrm{F}} = 1 \times 10^6\,\mathrm{m/s}$. Thus, one needs V^0_{CPD}. It can be deduced from $V_{\mathrm{CPD}}(x, y, V_{\mathrm{SD}} = 0\,\mathrm{V})$ maps recorded by EFM at charge neutrality, i.e., at $V_{\mathrm{gate}} = V_{\mathrm{D}}$, but not by KPFM.

For $V_{\mathrm{CPD}}(x, y)$ maps acquired by EFM, we then construct doping maps by applying eq. (S.13) straightforwardly. However, for KPFM, we have to consider that $V_{\mathrm{CPD}}(x, y)$ maps are obtained after subtracting a second order polynomial background (section) that largely removes the spatial average of $V_{\mathrm{CPD}}(x, y)$ (Fig. S9g). In order to restore the average, we calculate the average contact potential difference for a particular V_{gate} using $V_{\mathrm{CPD}} = V^0_{\mathrm{CPD}} + \mathrm{sign}(n_{\mathrm{gate}})\,\hbar v_{\mathrm{F}}\sqrt{\pi|n_{\mathrm{gate}}|}$ with $n_{\mathrm{gate}} = C_{\mathrm{gate}}\,(V_{\mathrm{gate}} - V_{\mathrm{D}})\,/e$ as doping density induced by the gate via a capacitive model (Fig. S9h). Subsequently, the histograms of the $V_{\mathrm{CPD}}(x, y)$

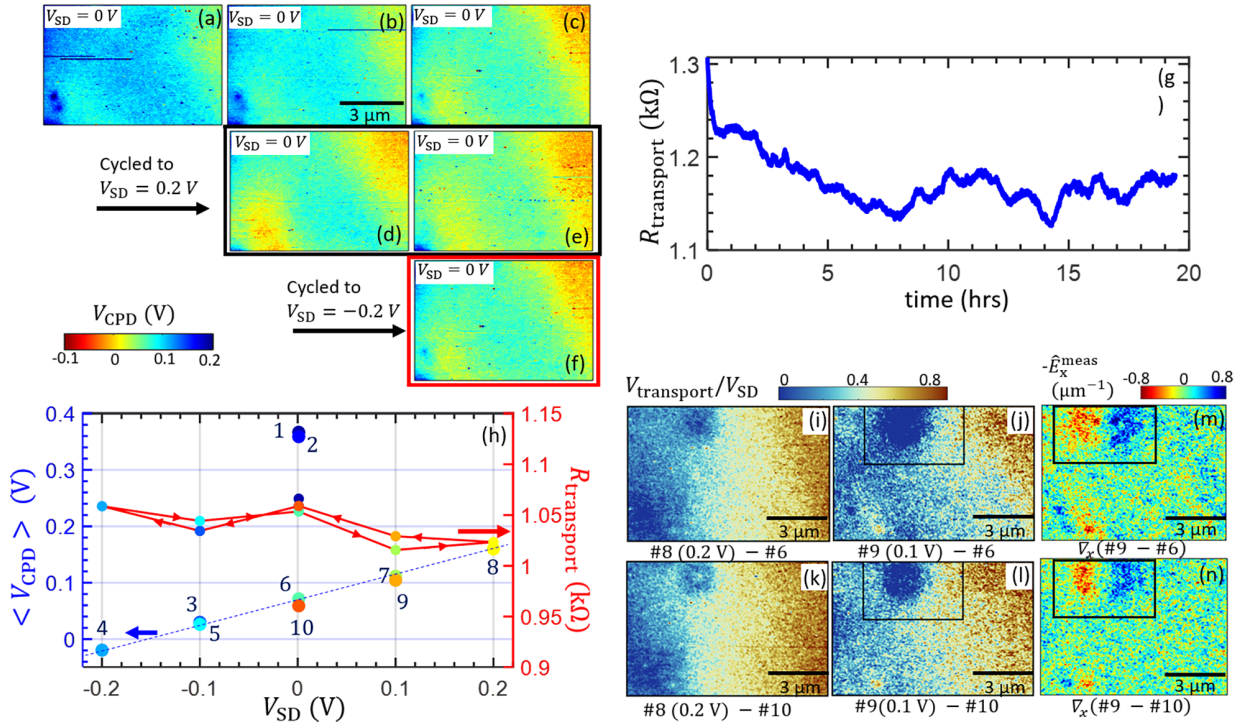

Figure S8: **Temporal Stability of Doping Distribution.** (a–f) Subsequently recorded $V_{\mathrm{CPD}}(x, y)$ maps using EFM, $V_{\mathrm{SD}} = 0\,\mathrm{V}$, $V_{\mathrm{gate}} = V_{\mathrm{D}} = 85\,\mathrm{V}$, $z_{\mathrm{tip}} = 20\,\mathrm{nm}$, $f_{\mathrm{drive}} = 61.7\,\mathrm{kHz}$, $V_{\mathrm{tip}} = 2\,\mathrm{V}$ during tapping mode traces, recording time per image: 34 min, waiting time prior to each image: $> 5\,\mathrm{min}$. V_{gate} and V_{SD} was changed one full day prior to the acquisition of a. Before recording d (f), V_{SD} was cycled to $+0.2\,\mathrm{V}$ ($-0.2\,\mathrm{V}$) staying there for 10 min. (g) Two terminal resistance $R_{\mathrm{transport}}$ recorded between the setting of V_{gate} and the data acquisition of Fig. 3, main text, $V_{\mathrm{gate}} = V_{\mathrm{D}} = 85\,\mathrm{V}$. (h) Spatially averaged V_{CPD} (larger dots, left axis) and simultaneously acquired temporarily averaged device resistance (smaller dots connected by red line, right axis) for a series of $V_{\mathrm{CPD}}(x, y)$ maps measured in order as numbered, just after finishing the time trace in g. Same colors belong to the same $V_{\mathrm{CPD}}(x, y)$ map. The current induced electric field map deduced from image 9 and image 6 (10) is also shown in Fig. 3e (f), main text. (i–l) $V_{\mathrm{transport}}(x, y)/V_{\mathrm{SD}}$ maps as deduced from the subtraction of the $V_{\mathrm{CPD}}(x, y)$ maps labelled in h as marked below each image (eq. (S.10)). Note that different reference maps at $V_{\mathrm{SD}} = 0\,\mathrm{V}$ are used for i, j and k, l. (m, n) Deduced $\widehat{E}_x^{\mathrm{meas}}(x, y)$ map (eq. (S.11)) from j and l, respectively, using the $V_{\mathrm{CPD}}(x, y)$ maps as marked below the image. The rectangular area marked in l–n is displayed in Fig. 3e, f main text

maps (Fig. S9a–c), i.e., each value of the map, are shifted such that the histogram maxima (Fig. S9g) are aligned with the calculated values of Fig. S9h. These adjusted $V_{\mathrm{CPD}}(x, y)$ maps are then used to apply eq. (S.13) resulting straightforwardly in the doping maps $n_0(x, y)$. Figure S9d-f displays resulting doping maps of the same area at different V_{gate}. The whole map changes from hole doping to electron doping due to the added V^0_{CPD}. Moreover, folds and wrinkles (topography in Fig. 5h, main text) charge less via gating, which is likely due to the larger distance from the gate.

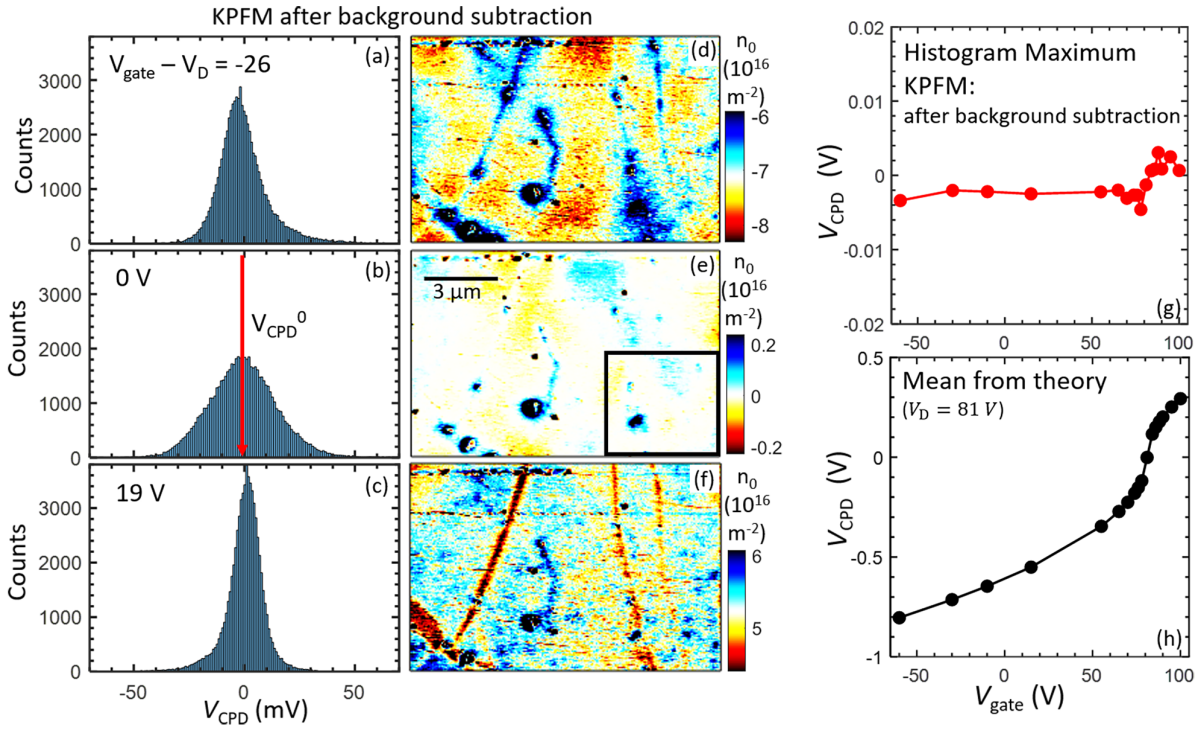

Figure S9: **Doping Maps.**(a–c) Histograms of $V_{\mathrm{CPD}}(x, y, V_{\mathrm{SD}} = 0\ \mathrm{V})$ as recorded by KPFM after background subtraction (section), $V_{\mathrm{gate}} - V_{\mathrm{D}}$ as marked, $V_{\mathrm{D}} = 81\,\mathrm{V}$, red line in b: deduced $V^0_{\mathrm{CPD}} = -1.3\,\mathrm{mV}$. (d–f) Doping maps $n_0(x, y)$ corresponding to the adjacent histograms and deduced from $V_{\mathrm{CPD}}(x, y, V_{\mathrm{SD}} = 0\ \mathrm{V})$ via eq. (S.13) using the capacitively calculated background shift of (h), corresponding topography: Fig. 5h, main text, black rectangle in e: region of Fig. 4a–f, main text. (g) Maximum of V_{CPD} histograms for various V_{gate} deduced from KPFM images after background subtraction. (h) $\langle V_{\mathrm{CPD}} \rangle$ as derived from a capacitive gating model ($V_{\mathrm{D}} = 81\,\mathrm{V}$, text) and as added to the background subtracted $V_{\mathrm{CPD}}(x, y)$ maps prior to applying eq. (S.13) for calculating $n_0(x, y)$.

Source Drain Induced Local Doping (SDILD)

As discussed in the main text, the doping distribution $n(x,y)$ is subject to a linear gradient at finite V_{SD}. The gate voltage reference at the graphene is ground for the drain electrode and shifted by V_{SD} with respect to ground for the source electrode (Fig. 2a, main text). Hence, we define a local gate voltage $V_{\mathrm{gate}}^{\mathrm{local}}(x,V_{\mathrm{SD}}) = V_{\mathrm{gate}} - \frac{V_{\mathrm{SD}}}{L}(x-x_0)$, where $x = x_0$ is the edge of the drain electrode and $x = 0$ the left side of the image (closest to the drain). We will use $V_{\mathrm{gate}}^{\mathrm{local}}(x,V_{\mathrm{SD}})$ to calculate the resulting $n(x,y)$ iteratively. Firstly, we regard the doping $n_0(x,y)$ at $V_{\mathrm{SD}} = 0\,\mathrm{V}$. Its fluctuations change the local charge neutrality point at finite V_{gate} reading $V_{\mathrm{D}}^{\mathrm{local}}(x,y) = V_{\mathrm{gate}} - e\frac{n_0(x,y)}{C_{\mathrm{eff}}(x,y,V_{\mathrm{SD}}=0\,\mathrm{V})}$. Here, $C_{\mathrm{eff}}(x,y,V_{\mathrm{SD}} = 0\,\mathrm{V}) = \left(\frac{1}{C_{\mathrm{gate}}} + \frac{1}{C_{\mathrm{Q}}(x,y,V_{\mathrm{SD}}=0\,\mathrm{V})}\right)^{-1}$ is the effective capacitance consisting of geometric capacitance C_{gate} and quantum capacitance $C_{\mathrm{Q}}(x,y,V_{\mathrm{SD}} = 0\,\mathrm{V}) = \frac{2e^2}{\pi}\frac{\sqrt{\pi|n_0(x,y)|}}{\hbar v_{\mathrm{F}}}$.

In a second step, we set up the iterative loop for $n(x,y)$ at finite V_{SD} reading

$$\begin{aligned} n(x,y,V_{\mathrm{SD}}) &= \frac{C_{\mathrm{eff}}(x,y,V_{\mathrm{SD}})}{e}\left(V_{\mathrm{gate}}^{\mathrm{local}}(x,V_{\mathrm{SD}}) - V_{\mathrm{D}}^{\mathrm{local}}(x,y)\right) \\ &= \frac{C_{\mathrm{eff}}(x,y,V_{\mathrm{SD}})}{C_{\mathrm{eff}}(x,y,V_{\mathrm{SD}}=0\,\mathrm{V})}n_0(x,y) - \left(\frac{V_{\mathrm{SD}}}{eL}\right)C_{\mathrm{eff}}(x,y,V_{\mathrm{SD}})(x-x_0), \end{aligned} \tag{S.14}$$

where $C_{\mathrm{eff}}(x,y,V_{\mathrm{SD}})$ is the effective capacitance for the changed doping $n(x,y,V_{\mathrm{SD}})$ via V_{SD}. Thus, both sides of the equation depend on $n(x,y,V_{\mathrm{SD}})$ suggesting a self-consistent loop that we applied for solving. Far away from charge neutrality, the second term is negligible, since $|V_{\mathrm{SD}}| \ll V_{\mathrm{gate}}$ and $C_{\mathrm{eff}}(x,y,V_{\mathrm{SD}}) \approx C_{\mathrm{gate}}$ implying $n(x,y) \approx n_0(x,y)$, i.e., SDILD is negligible. However, when $V_{\mathrm{gate}} \to V_{\mathrm{D}}$, the first term is almost zero raising the importance of the second term. Consequently, V_{SD} induced gating (SDILD) has to be considered carefully, in particular, close to charge neutrality.

Electric Field from SDILD

In section , we assigned the difference between biased and unbiased $V_{\mathrm{CPD}}(x,y)$ maps to the current induced voltage drop $V_{\mathrm{transport}}(x,y)$ (eq. (S.10)) using the assumption that the doping distribution in the sample remains unchanged. However, section reveals that V_{SD} changes the doping via SDILD (eq. (S.14)), most strongly close to charge neutrality. Even for a linear potential drop along the sample by V_{SD}, we get non-linearities in $V_{\mathrm{transport}}(x,y)$ (eq. (S.10)) via the non-linear local doping due to quantum capacitance (eq. (S.14)). We dub the resulting electric field via SDILD $\mathbf{E}^{\mathrm{SDILD}}(x,y)$ (eq. S.11). Here, we present a formalism to calculate it for known V_{SD} and $n_0(x,y)$ (eq. S.13). A comparison of $\mathbf{E}^{\mathrm{SDILD}}(x,y)$ with $\mathbf{E}^{\mathrm{meas}}(x,y)$ then allows to distinguish between non trivial transport features and those due to SDILD.

The Fermi energy of graphene reads $E_{\mathrm{F}} - E_{\mathrm{D}} = \hbar v_{\mathrm{F}}\,\mathrm{sign}(n)\sqrt{\pi|n|}$ with $n(x,y,V_{\mathrm{SD}})$ being the doping distribution including SDILD (eq. (S.14)). If we assume that the applied V_{SD} drops linearly along the graphene, implying a potential $\frac{V_{\mathrm{SD}}}{L}(x-x_0)$ (x_0: edge of the drain electrode), we obtain

$$\begin{aligned} V_{\mathrm{CPD}}(x,y,V_{\mathrm{SD}}) &= V^0_{\mathrm{CPD}} + \frac{(E_{\mathrm{F}}(x,V_{\mathrm{SD}}) - E_{\mathrm{D}}(x,y,V_{\mathrm{SD}}))}{|e|} + \frac{V_{\mathrm{SD}}}{L}(x-x_0) \\ &= V^0_{\mathrm{CPD}} + \frac{\hbar v_{\mathrm{F}}}{|e|}\,\mathrm{sign}(n(x,y,V_{\mathrm{SD}}))\sqrt{\pi|n(x,y,V_{\mathrm{SD}})|} + \frac{V_{\mathrm{SD}}}{L}(x-x_0). \end{aligned} \tag{S.15}$$

The contact potential difference in the unbiased case is (section)

$$V_{\mathrm{CPD}}(x,y,0) = V^0_{\mathrm{CPD}} + \frac{\hbar v_{\mathrm{F}}}{|e|}\mathrm{sign}(n_0(x,y))\sqrt{\pi|n_0(x,y)|}.$$

The resulting x component of the electric field (eqs. (S.10), (S.11)) becomes

$$
\begin{aligned}
E_x^{\mathrm{SDILD}}(x,y,V_{\mathrm{SD}}) &= -\frac{d}{dx}[V_{\mathrm{CPD}}(x,y,V_{\mathrm{SD}}) - V_{\mathrm{CPD}}(x,y,0)] \\
&= -\frac{V_{\mathrm{SD}}}{L} - \frac{\hbar v_{\mathrm{F}}}{|e|}\frac{d}{dx}[\mathrm{sign}(n(x,y,V_{\mathrm{SD}}))\sqrt{\pi|n(x,y,V_{\mathrm{SD}})|} - \mathrm{sign}(n_0(x,y))\sqrt{\pi|n_0(x,y)|}] \\
&= E_x^0 - \frac{\hbar v_{\mathrm{F}}\sqrt{\pi}}{2|e|}\left(\frac{1}{\sqrt{|n(x,y,V_{\mathrm{SD}})|}}\frac{dn(x,y,V_{\mathrm{SD}})}{dx} - \frac{1}{\sqrt{|n_0(x,y)|}}\frac{dn_0(x,y)}{dx}\right),
\end{aligned}
\tag{S.16}
$$

using $\frac{d}{dx}\left(\mathrm{sign}(n)\,\sqrt{\pi|n|}\right) = \frac{\sqrt{\pi}}{2}\frac{1}{\sqrt{|n|}}\frac{dn}{dx}$. The term $E_x^0 = -V_{\mathrm{SD}}/L$ is the trivial electric field by the linear voltage drop due to V_{SD}. Normalising the electric field to V_{SD}, we get

$$
\begin{aligned}
\widehat{E}_x^{\mathrm{SDILD}}(x,y,V_{\mathrm{SD}}) &= -\frac{1}{L} - \frac{\beta}{V_{\mathrm{SD}}}\left(\frac{1}{\sqrt{|n(x,y,V_{\mathrm{SD}})|}}\frac{dn(x,y,V_{\mathrm{SD}})}{dx} - \frac{1}{\sqrt{|n_0(x,y)|}}\frac{dn_0(x,y)}{dx}\right) \\
&:= \widehat{E}_x^0 - \frac{\beta}{V_{\mathrm{SD}}}\chi(x,y,V_{\mathrm{SD}})
\end{aligned}
\tag{S.17}
$$

with $\beta = \hbar v_{\mathrm{F}}\sqrt{\pi}/2|e| = 6.425 \cdot 10^{-10}\,V\mathrm{m}$ and $\widehat{E}_x^0 = -1/L \approx -0.055\,\mu\mathrm{m}^{-1}$.

Obviously, $\widehat{E}_x^{\mathrm{SDILD}}$ diverges, if $n_0(x,y)$ or $n(x,y,V_{\mathrm{SD}})$ crosses zero as naturally appearing close to charge neutrality. This implies pronounced local maxima and minima in the measured electric field maps that are not caused by the current flow.

As an example, we consider a one-dimensional parabolic profile $n_0(x)$ along x with negative curvature crossing zero twice and being located in the center between source and drain electrode (black line, Fig. S10a). Applying V_{SD} results in a vertical and horizontal shift (grey line, Fig. S10a).The vertical shift is more pronounced than the horizontal one, since the total length within Fig. S10a is much smaller than the distance to the drain electrode. Since the drain is grounded, half of the V_{SD} induced potential drops towards the displayed center region. Naturally, the two zero crossings of the $n(x)$ parabola are shifted inwards with respect to the zero crossings of $n_0(x)$ such that eq. (S.17) implies four distinct diver-

gences of $\widehat{E}_x^{\mathrm{SDILD}}(x)$ along x. The direction of divergence, peak or dip, changes between the zeroes of $n(x)$ and the zeroes of $n_0(x)$ at the same slope of the parabola (eq. (S.17)). It also changes with direction of slope for the same density, either $n(x)$ or $n_0(x)$. Consequently, a quadrupole of $\widehat{E}_x^{\mathrm{SDILD}}(x)$ divergences appears for the inverted $n_0(x)$ parabola with order dip-peak-dip-peak from left to right (red line, Fig. S10a). Quantum capacitance barely changes this scenario (full and dashed grey line, Fig. S10a).

Figure S10b shows a 2D plot of $\widehat{E}_x^{\mathrm{SDILD}}(x, y)$ for a rotationally symmetric parabolic doping profile $n_0(x, y)$ with the same apex and curvature as in Fig. S10a. It features four lobes, one for each of the four divergences that we have already discussed in Fig. S10a. The inner lobes appear more extended along x than the outer lobes as consequence of the weaker slopes $dn(x, y)/dx$ at the zeroes of $n(x, y)$ compared to the stronger slopes $dn_0(x, y)/dx$ at the zeroes of $n_0(x, y)$.

Figure S10c displays an $\widehat{E}_x^{\mathrm{SDILD}}(x, y)$ map deduced from a measured $V_{\mathrm{CPD}}(x, y, V_{\mathrm{SD}} = 0\,\mathrm{V})$ map by KPFM using eqs. (S.13), (S.14) and (S.16). For comparison, the measured $\widehat{E}_x^{\mathrm{meas}}(x, y)$ map of the same area is displayed in Fig. S10d. The features that are similar in both images (red arrows) are attributed to artifacts from SDILD, while additional features in the $\widehat{E}_x^{\mathrm{meas}}(x, y)$ map, such as the encircled yellowish area of inverted electric field, can be assigned to current induced features.

Simulation of the Measured Electric Fields in Fig. 3 by SDILD

Figure 3e, f, main text, showcase a dipolar $\widehat{E}_x^{\mathrm{meas}}(x, y)$ structure as determined by EFM that exhibits a spatial extent and an intensity of its two lobes much larger than the apparent electric field generated by SDILD (Fig. 3c, d, main text). This structure is shown again in Fig. S12e. Since we can not avoid temporal fluctuations of the doping profile $n_0(x, y)$ completely (section), we also attempted to reproduce the recorded dipolar $E_x^{\mathrm{meas}}(x, y)$ structure by an arbitrary, artificial doping profile $n_0(x, y)$. Eventually, we found such a doping profile (black line, Fig. S12d) that, however, appears to be impossible in reality. We describe the

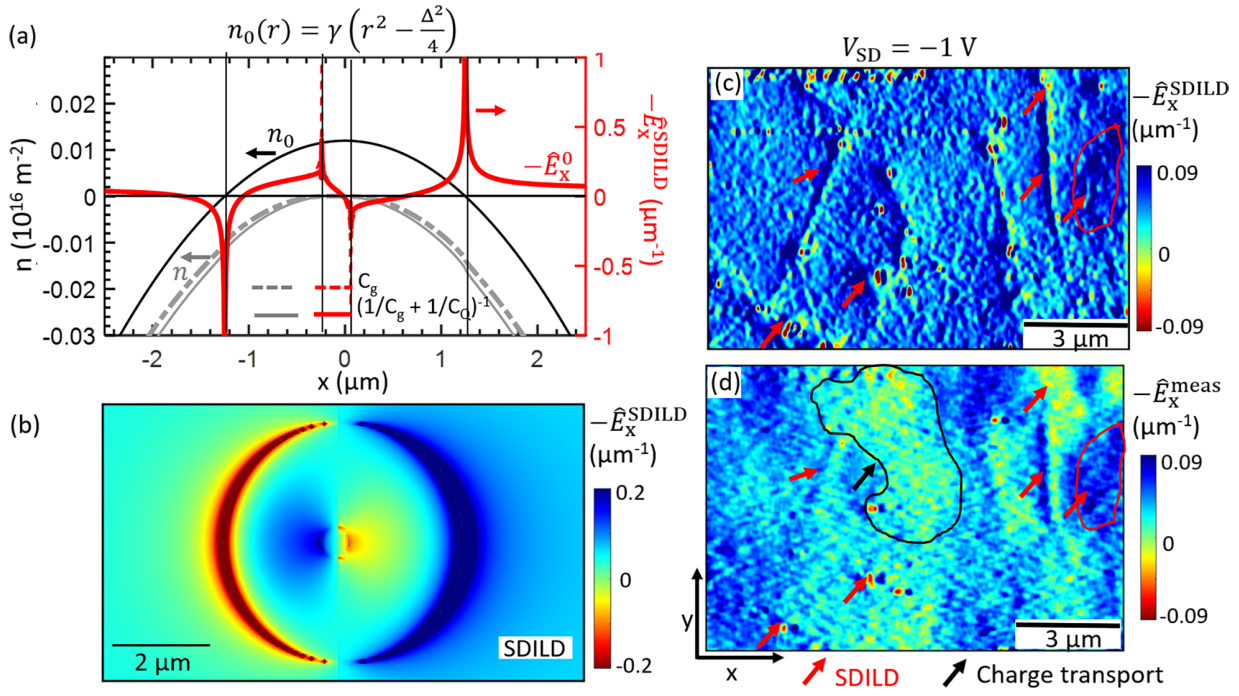

Figure S10: **Electric fields from SDILD.** (a) Doping profiles (left axis): parabolic $n_0(x)$ at $V_{SD} = 0\,V$ (black line) using the equation above with $\Delta = 2.5\,\mu m$, $\gamma = -8.3 \cdot 10^{25}\,m^{-4}$ and resulting $n(x, V_{SD} = 0.1\,V)$ (grey lines) according to eq. (S.14) either neglecting quantum capacitance (dashed line) or including it (full line). In addition, the deduced $\widehat{E}_x^{SDILD}(x)$ (red line, right axis) is shown using eq. (S.17) without quantum capacitance (dashed) or with it (full). Dashed red line: trivial $\widehat{E}_x^0 = -1/L = -0.055\,\mu m^{-1}$ resulting from the device geometry. (b) 2D color map of $\widehat{E}_x^{SDILD}(x, y, V_{SD} = 0.1\,V)$ for a rotational symmetric parabolic doping profile (formula and parameters as in a) located in the center between source and drain electrode. The trivial field $\widehat{E}_x^0$ has been subtracted. (c) $\widehat{E}_x^{SDILD}(x, y, V_{SD})$ map calculated from a measured $V_{CPD}(x, y, V_{SD} = 0\,V)$ map (AM KPFM) at charge neutrality ($V_{gate} = 72\,V$) for $V_{SD} = -1\,V$. (d) Measured $\widehat{E}_x^{meas}(x, y)$ of the same area as c (same as Fig. 5p, main text). The red arrows in c,d mark features present in both images and, hence, attributed to SDILD. The black arrow in d points at an encircled feature not present in c, and, hence, assigned to the current flow.

reasoning in the following after recalling that the doping profiles recorded prior and after the $V_{\mathrm{CPD}}(x, y, V_{\mathrm{SD}} = 0.1\,\mathrm{V})$ map necessary for $E_x^{\mathrm{meas}}(x, y)$ are, both, not capable to reproduce $E_x^{\mathrm{meas}}(x, y)$ via SDILD (Fig. 3, main text).

We firstly consider a one dimensional doping profile $n_0(x)$ and later extend the analysis to two dimensions. To observe a divergence of the electric field via SDILD, either $n_0(x)$ or $n(x)$ must cross zero (eq. (S.17)). As shown in Fig. S10a–b, $\widehat{E}_x^{\mathrm{SDILD}}$ rapidly decreases away from such crossings. Hence, we firstly focus on the area close to such crossings. If, both, $n_0(x)$ and the shifted $n(x)$ cross zero with the same direction of slope, one gets a dipolar divergence of $\widehat{E}_x^{\mathrm{SDILD}}(x)$ (Fig. S10a). Around the crossing point, we apply a Taylor expansion of $n_0(x)$ and $n(x)$, here given for $n_0(x)$ around a crossing at $x = 0$, to deduce leading terms reading

$$n_0(x) = \sum_m \alpha_m \left(\frac{x}{L}\right)^m, \;\; m = 1, 2, 3..... \tag{S.18}$$

Here, m is an integer exponent, α_m the corresponding prefactor and L a constant length. Considering eq. (S.17), we find for the individual terms of the expansion

$$\frac{dn_0(x)/dx}{\sqrt{n_0(x)}} = \frac{m\sqrt{\alpha_m}}{L} \cdot \left(\frac{x}{L}\right)^{m/2-1}. \tag{S.19}$$

Consequently, the linear term of the expansion ($m = 1$) produces the divergence, while the other terms contribute (in first order) by zero ($m > 2$) or $m\sqrt{\alpha_m}/L$ ($m = 2$) to $\widehat{E}_x^{\mathrm{SDILD}}(x)$ at the crossing point. Thus, the width of the prominent SDILD feature around $n_0(x) = 0$ is largely dominated by the linear term of the Taylor expansion (see discussion below for the influence of higher order terms). A resulting dipolar $\widehat{E}_x^{\mathrm{SDILD}}(x)$ for a linear $n_0(x)$ term, as calculated numerically via eq. (S.17), is shown in Fig. S11a. It exhibits a very small width w_{lobe} of its two lobes at the required strength $|\widehat{E}_x^{\mathrm{SDILD}}(x)| > 0.25/\mu\mathrm{m}$ that has been found in the experiment (Fig. S12e). This width w_{lobe} in x direction, where $|\widehat{E}_x^{\mathrm{SDILD}}(x)| > 0.25/\mu\mathrm{m}$, is plotted as a function of the linear prefactor α_1 in Fig. S11f (pink lines) revealing a maximum of w_{lobe} for both lobes (dashed, full line). Thus, albeit the extremal $|\widehat{E}_x^{\mathrm{SDILD}}(x)|$ increases

monotonously with α_1 (Fig. S11e), w_{lobe} is non-monotonous with a maximum at $w_{\mathrm{lobe}} \approx 0.1\,\mu$m, exactly for the $n_0(x)$ slope as used in Fig. S11a. Thus, a linear zero crossing of $n_0(x)$ can not reproduce the width of the experimentally observed $\widehat{E}_x^{\mathrm{meas}}(x)$ dipolar feature with $w_{\mathrm{lobe}} \simeq 1.7\,\mu$m. Numerical tests of various shapes around the $n_0(x) = 0$ crossing corroborated this result for more general crossings within reasonable limits.

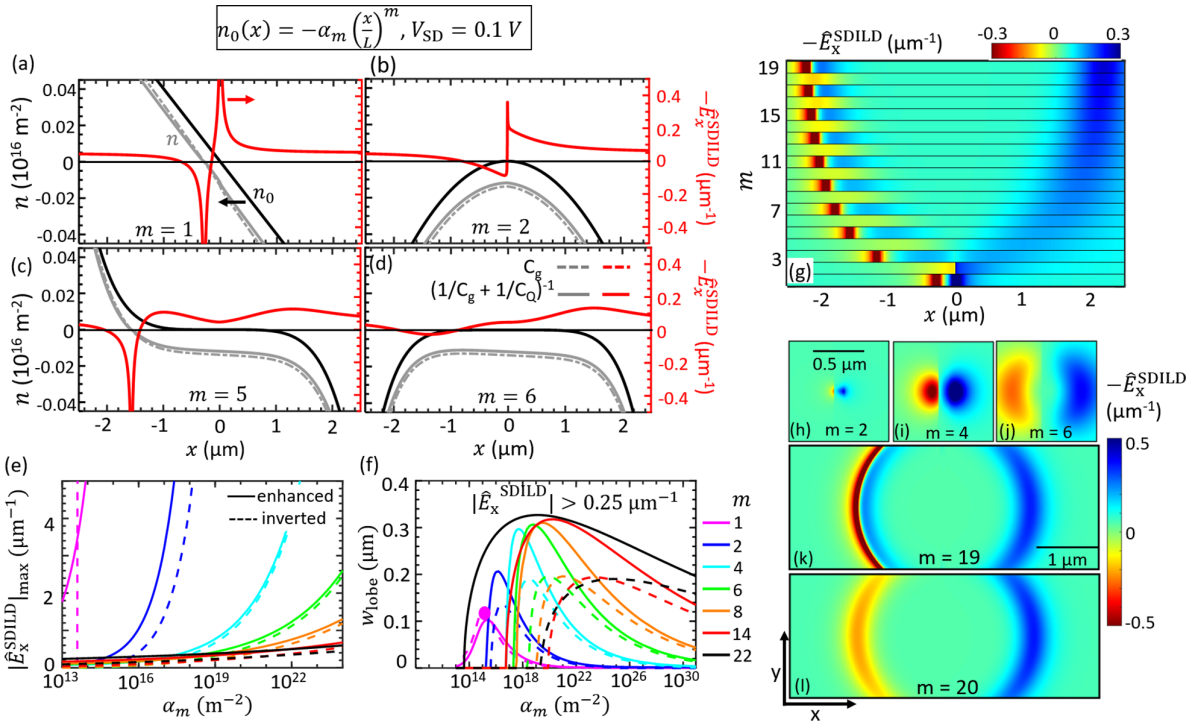

Figure S11: $\widehat{E}_x^{\mathrm{SDILD}}(x, y)$ **for different exponents of** $n_0(x, y)$**.** (a–d) Simulated doping profiles $n_0(x)$ (black lines) according to the formula on top with $\alpha_m = 1 \cdot 10^{15}/\mathrm{m}^2$ and $n(x)$ at $V_{\mathrm{SD}} = 0.1\,\mathrm{V}$ (grey lines) according to eq. (S.14) for different exponents m as marked (left axis). The resulting electric field from SDILD $\widehat{E}_x^{\mathrm{SDILD}}(x)$ according to eq. (S.17) is drawn in red (right axis). Full (dashed) lines include (do not include) quantum capacitance. (e) Extremal electric field within the two lobes of the simulated dipolar structures (as shown in a, c, d) for different m. Solid and dashed lines refer to the lobe with enhanced and inverted electric field, respectively. (f) Width along x of the simulated two lobes with $|\widehat{E}_x^{\mathrm{SDILD}}(x, y)| \geq 0.25\,\mu$m. Large pink dot marks the width deduced from a. (g) $\widehat{E}_x^{\mathrm{SDILD}}(x)$ for different m using $n_0(x)$ as given above a, b, $\alpha_m = 1 \cdot 10^{15}/\mathrm{m}^2$. (h–l) $\widehat{E}_x^{\mathrm{SDILD}}(x, y) - \widehat{E}_x^0$ (eq. (S.17)) for different exponents m as marked using a rotational symmetric $n_0(|\vec{x}|)$ with radial dependence as given above a, b, $\alpha_m = 5 \cdot 10^{18}/\mathrm{m}^2$ (b), h–j have the same size, k–l have the same size. All images use $V_{\mathrm{SD}} = 0.1\,\mathrm{V}$.

As alternative, we consider $n_0(x)$ functions that are touching $n_0(x) = 0$ with zero slope

$dn_0(x)/dx = 0$ (argument applies analogously for $n(x)$). Again, we apply a Taylor expansion of $n_0(x)$ around $n_0(x) = 0$. This also adresses the higher order terms of the zero crossings on the same footing. We realize that the odd powers of the Taylor expansion with $m > 1$ cannot produce a dipolar structure at all (Fig. S11c), while for $m = 1$ the same argument as above applies. As illustrated for $m = 5$ in Fig. S11c, the functions with odd exponent $m > 1$ produce a strong divergence of $\widehat{E}_x^{\mathrm{SDILD}}(x)$ at the shifted $n(x) = 0$ due to its large slope $|dn/dx|$. In addition, two weaker features appear that are symmetric around the touching point $n_0(x) = 0$. These two weaker features originate from $n_0(x)$ and naturally exhibit the same strength on both sides of $n_0(x) = 0$ and the same distance from $x = 0$ (eq. (S.17)). Thus, each odd power produces either a monopolar or a tripolar structure, but not a dipolar one as crosschecked numerically. In contrast, the even powers of $n_0(x)$ result in an antisymmetric $\widehat{E}_x^{\mathrm{SDILD}}(x)$ feature around the touching point provided that $n(x)$ is moved completely away from $n(x) = 0$ via V_{SD} (Fig. S11b,d). Hence, a dipolar structure naturally appears for an even power function of $n_0(x)$ ($n(x)$) with negative (positive) curvature in case of the applied positive V_{SD}. However, numerically, it turns out that also the lobes of these dipolar $\widehat{E}_x^{\mathrm{SDILD}}(x)$ structures exhibit a maximum width of $0.3\,\mu$m at the required $\widehat{E}_x^{\mathrm{SDILD}} > 0.25/\mu$m (Fig. S11f). This is again much too small to reproduce the experiment (Fig. S12e).

However, the numerical analysis of the different exponents reveals that the extrema of the dipolar (even m) and tripolar (odd $m > 1$) $\widehat{E}_x^{\mathrm{SDILD}}(x)$ structures move continuously outwards with increasing m. This is displayed in Fig. S11g showing $\widehat{E}_x^{\mathrm{SDILD}}(x)$ profiles for each exponent m, in this case using $\alpha_m = 1 \cdot 10^{15}/\mathrm{m}^2$ independent of m. The systematic shift to larger distances with m is due to the increasingly flat $n_0(x)$ part in the center (Fig. S11a–d). While eq. (S.19) indicates a continuously increasing $\widehat{E}_x^{\mathrm{SDILD}}(x)$ with increasing $|x|$ and increasing m, this increasing strength due to $n_0(x)$ gets increasingly compensated by the additional $n(x)$ term in eq. (S.17). Basically, the offset between $n_0(x)$ and $n(x)$ within the square root denominators looses its importance. Very roughly, the extrema appear at the x

positions, where $n_0(x)$ has a similar value than $n(x = 0)$. This naturally explains that the extrema move outwards with increasing m. Nevertheless, its width w_{lobe} always remains far below the experimental $w_{\text{lobe}} \simeq 1.7\mu$m (Fig. S11f). In addition, Fig. S11g nicely shows the alternating tripolar and dipolar structures for increasing m.

The extension to 2D isotropic profiles does not change the above arguments as shown exemplarily in Fig. S11h–l.

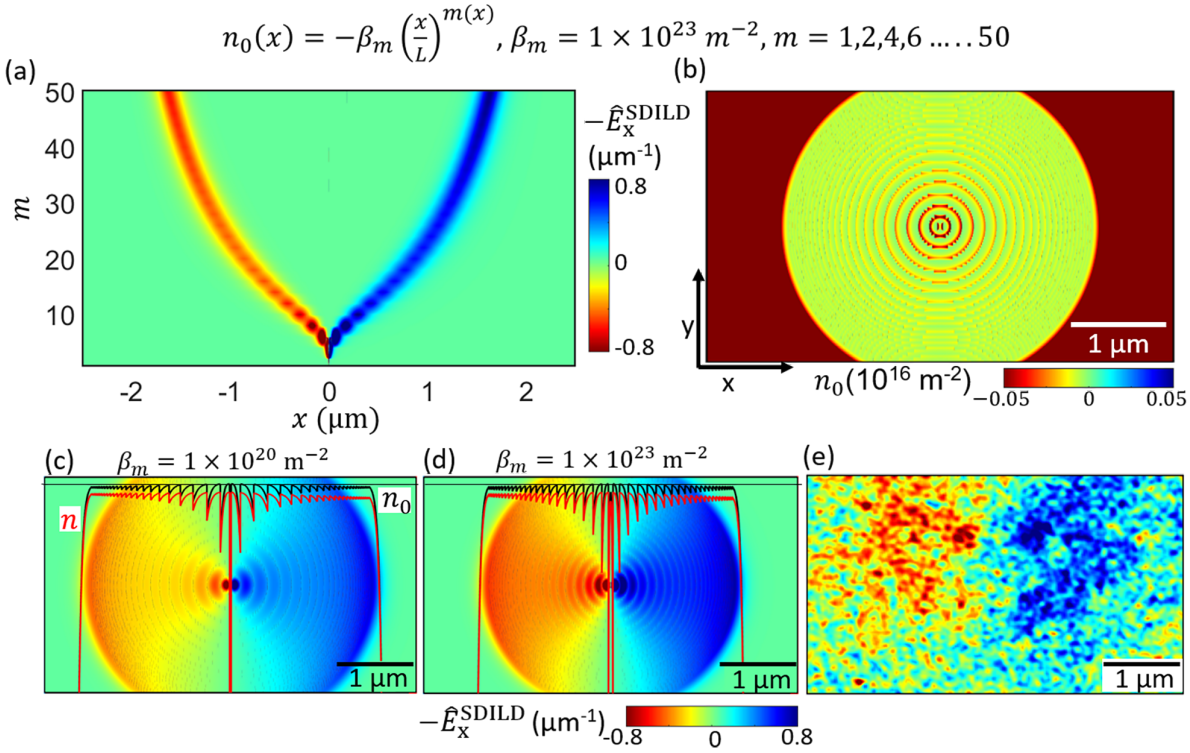

Figure S12: **Patching doping profiles to reproduce $\widehat{E}_x^{\text{meas}}(x, y)$ by SDILD.** (a) $\widehat{E}_x^{\text{SDILD}}(x)$ at $V_{\text{SD}} = 0.1\,\text{V}$ for different exponents m of the employed $n_0(x)$ function given on top using eqs. (S.14), (S.17). The vertical lines mark x sections that are patched with a singular exponent m in eq. (S.20) with m increasing symmetrically from the center to the rims of the x axis. In particular, the section at $x = 0$ exhibits $m = 1$, the two adjacent ones $m = 2$, the two next outer ones $m = 4$, etc.. (b) Doping distribution $n_0(x, y)$ using eq. (S.20) and the patched m sequence as marked/described in a, but rotational symmetric. (c–d) $\widehat{E}_x^{\text{SDILD}}(x, y)$ using $n_0(x, y)$ from b, but with different constant β_m as marked, according to eqs. (S.14), (S.17). Black and red curves are cross sections through the doping profiles $n_0(x, y = 0)$ and $n(x, y = 0, V_{\text{SD}})$ along x at the center of the image (right axis). (e) $\widehat{E}_x^{\text{meas}}(x, y)$ at $V_{\text{SD}} = 0.1\,\text{V}$ via eq. (S.12), (S.10) (same as Fig.3e, main text), same colorbar for c–e.

Since the single components of the Taylor series are not able to reproduce inverted field lobes of intensity above $0.25\,\mu\mathrm{m}^{-1}$ and width $w_{\mathrm{lobe}} > 1.7\,\mu\mathrm{m}$, we have to patch $n_0(x)$ piecewise in order to get a large enough width of the dipolar structure. Since a patched sequence of crossings would produce a sequence of dipolar structures via their dominating linear term instead of a single extended dipolar structure, the option of patching crossing points does not exist.

The fact that the extrema of the dipolar structure for each even m shift outwards with increasing m (Fig. S12a) suggests a natural way of patching by choosing x ranges of extremal $\widehat{E}_x^{\mathrm{SDILD}}$ for each even m until the extrema position of the largest m matches the x extension of the experimental dipolar $\widehat{E}_x^{\mathrm{meas}}(x, y)$ structure. More formally, we use

$$n_0(x) = -\beta_m \cdot \left(\frac{x}{L}\right)^{m(x)} \tag{S.20}$$

with $m(x)$ being a step function that is a piecewise constant integer along x, featuring subsequently $m = 1, 2, 4, 6, 8, ...$ and using $L = 2.5\,\mu\mathrm{m}$ (Fig. S12a,b). Increasing the parameter β_m tunes the intensity of the dipolar structure (Fig. S11e), but increases the number of required patches simultaneously by decreasing w_{lobe} (Fig. S11f). Using this construction, we found that ~ 50 patches are required to reproduce the width and strength of the experimentally observed dipolar structure (Fig. S12d, e). However, this necessarily requires that each area of different m is adjusted to $n_0(x) = 0/\mathrm{m}^2$ in the center (at $x = 0$) implying jumps of $n_0(x)$ as displayed by the black line in Fig. S12d. It implies ~ 50 jumps in $n_0(x)$ on a width of $3\,\mu\mathrm{m}$ (lines in Fig. S12d). Each jump returns $n_0(x)$ basically back to zero. Such doping profiles are experimentally very unlikely, in particular, to be present in a certain region but not in its surrounding.

Importantly, albeit different patching profiles might reproduce the experimental dipolar structure, the patching method with its multiple jumps back to $n_0(x) \approx 0$ cannot by avoided. Any type of a smooth return to $n_0(x) \approx 0$ would lead to the opposite electric field such that

instead of an extended lobe, one would get multiple dipolar structures within the lobe area. The resulting requirement of the jumps strongly excludes a physical possibility that the observed dipolar structure is caused by SDILD, even in the unlikely case that the doping profile during recording $V_{\mathrm{CPD}}(x, y, V_{\mathrm{SD}})$ is substantially different from the one prior and after the recording.

Estimates of Local Scattering Lengths

Electron Electron Scattering Length l_{ee}

The electron-electron scattering length l_{ee} is associated with the quasiparticle decay rate τ_{ee}^{-1} due to inelastic electron electron scattering via $l_{\mathrm{ee}} = v_{\mathrm{F}}\tau_{\mathrm{ee}}$. This is directly related to the imaginary part of the retarded self energy $\Sigma_s^{\mathrm{R}}(\mathbf{k}, \xi_{\mathbf{k},\mathrm{s}})$ of monolayer graphene as[71]

$$\frac{1}{\tau_{\mathrm{ee}}} = 2\,\mathrm{Im}\left[\Sigma_s^{\mathrm{R}}(\mathbf{k}, \xi_{\mathbf{k},\mathrm{s}}),\right] \tag{S.21}$$

where $s = +/-$ is the conduction/valence band index and $\xi_{\mathbf{k},\mathrm{s}} = s\hbar v_{\mathrm{F}}|\mathbf{k}| - \mu$ is the single particle band energy relative to the non-interacting chemical potential μ at finite temperature. Since graphene on SiN is a weakly correlated material (interaction parameter $r_{\mathrm{s}} = 0.51$),[54] the GW approximation is adequate[50] leading to[72]

$$\begin{aligned}\mathrm{Im}[\Sigma_s^{\mathrm{R}}(k,\omega)] = \sum_{\mathbf{q},s'=\pm} V_q \left[n_{\mathrm{B}}\left(\xi_{\mathbf{k}+\mathbf{q},\,s'} - \hbar\omega\right) + n_{\mathrm{F}}\left(\xi_{\mathbf{k}+\mathbf{q},\,s'} - \hbar\omega\right)\right] \\ \times (1 + ss'\cos\theta)\,\mathrm{Im}\left[\frac{1}{\epsilon\left(q, \xi_{\mathbf{k}+\mathbf{q},\,s'}/\hbar - \omega\right)}\right],\end{aligned} \tag{S.22}$$

where $V_q = \frac{2\pi e^2}{\kappa q}$ is the Coulomb interaction for momentum transfer q, $\kappa = 4.25$ is the background dielectric constant combining SiN and vacuum, n_{B} and n_{F} are the Bose and Fermi distribution functions, respectively, and θ is the angle between electron wave vectors $\mathbf{k}$ and

$\mathbf{k}+\mathbf{q}$. The finite temperature dynamic dielectric function $\epsilon(q,\omega)$ reads within Random Phase Approximation (RPA) $\epsilon(q,\omega) = 1 + V_q\Pi(q,\omega)$, where $\Pi(q,\omega)$ is the irreducible polarizability.

In the limit of small ξ_k and low temperature, $\xi_\mathbf{k} \ll k_\mathrm{B}T \ll E_\mathrm{F}$, where $E_\mathrm{F} = \hbar v_\mathrm{F} \cdot \mathrm{sign}(n)\sqrt{\pi|n|}$ is the Fermi energy for charge carrier density n, an asymptotic form of eq. (S.22) has been derived by Li et al.[55] (eq. (10), there), that by substituting into eq. (S.21) results in an electron-electron scattering length l_ee:[26,51,52]

$$l_\mathrm{ee} = \frac{4}{\pi}\left(\frac{\hbar v_\mathrm{F}}{k_\mathrm{B}T}\right)^2 \sqrt{\pi|n|}\frac{1}{\ln\left(\frac{2E_\mathrm{F}}{k_\mathrm{B}T}\right)} \tag{S.23}$$

as also given as eq. (4), main text. For the gate voltages of Fig. 4g, main text, where $l_\mathrm{ee}(V_\mathrm{gate})$ is plotted for $T = 298\,\mathrm{K}$, we have $k_\mathrm{B}T/E_\mathrm{F} \in [0.08 - 0.24]$, except at charge neutrality, such that the required limit of eq. (S.23) applies.[55]

The formalism is, moreover, not applicable in the quantum critical regime that appears at room temperature for carrier concentrations $n < 1.5 \times 10^{14}\,\mathrm{m}^{-2}$,[53] far lower than n for all data points in Fig. 4g, main text, and Fig. S14e, except of charge neutrality. But even at charge neutrality, the lateral charge fluctuations $\delta n_\mathrm{dis} \approx 1 \times 10^{15}\,\mathrm{m}^{-2}$ (puddles) are one order of magnitude larger than the threshold for quantum criticality. Finally, the threshold carrier concentration n_thermal above which eq. (S.23) is valid ($E_\mathrm{F}(n_\mathrm{thermal}) = k_\mathrm{B}T$) is $n_\mathrm{thermal} \approx 5 \times 10^{14}\,\mathrm{m}^{-2}$, i.e., larger than the quantum critical threshold, but lower than δn_dis.

Electron Disorder Scattering Length l_dis

All scattering processes of electrons with external perturbations as point defects, Coulomb type impurities, sample edges, or phonons change the momentum of the electron system. We dub the respective scattering length l_dis (disorder scattering length). A straightforward approach to determine l_dis uses the resistivity of graphene at high carrier densities where electron-electron scattering is negligible (eq. (S.23)), such that the effective mean free path

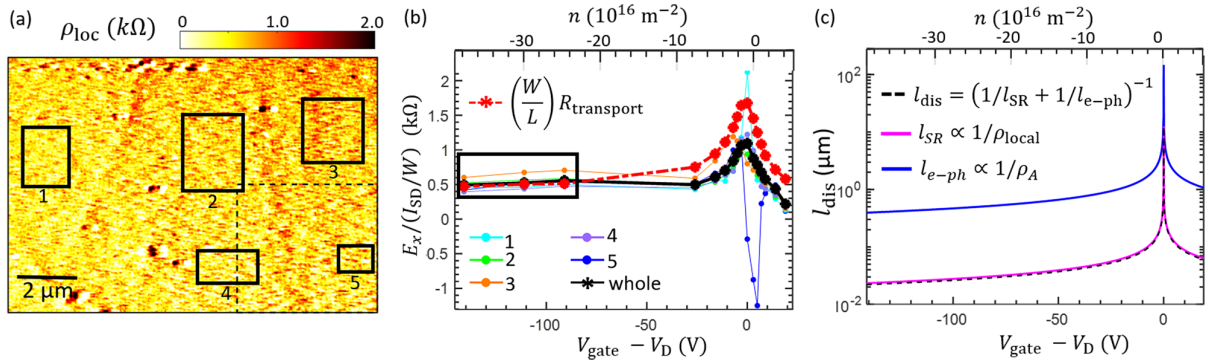

Figure S13: **Disorder Scattering Length.** (a) Map of local resistivity $\rho_{\mathrm{loc}}(x,y) = \langle E_x^{\mathrm{meas}}(x,y,V_{\mathrm{gate}},V_{\mathrm{SD}}=0.4\,\mathrm{V})\rangle_{V_{\mathrm{gate}}}/(I_{\mathrm{SD}}/W)$ with $E_x^{\mathrm{meas}}(x,y)$ averaged for $V_{\mathrm{gate}} = -141 - -91\,\mathrm{V}$ (rectangle in b), I_{SD}: source-drain current during imaging, W: sample width, respective topography: Fig. 5h, main text. Black rectangles mark the spatial averaging areas for the data in b. (b) Spatially averaged $\overline{\rho}_{\mathrm{loc}}(V_{\mathrm{gate}}) = \langle E_x^{\mathrm{meas}}(x,y,V_{\mathrm{SD}}=0.4\,\mathrm{V},V_{\mathrm{gate}})\rangle_{x,y}/(I_{\mathrm{SD}}/W)$. Full colored lines: areas marked in a, black line: whole region of a, red dashed line: two-terminal device resistivity, L: sample length. (c) Simulated V_{gate} dependence (eq. S.24) of the electron-phonon scattering length $l_{\mathrm{e-ph}}$ due to gate independent resistivity $\rho_{\mathrm{A}} = 30\,\Omega$ from longitudinal accoustic phonon scattering[55,73] (blue) and the complete electron disorder scattering length l_{dis} deduced from the measured $\rho_{\mathrm{local}} = 500\,\Omega$ at large $|V_{\mathrm{gate}}|$ (dashed black) as well as the resulting short range disorder scattering length l_{SR} (magenta) employing the Matthiesen rule shown as inset. The upper electron density axis (n) in b and c is deduced from a capacitive model.

reading $l_{\mathrm{MFP}} = \left(l_{\mathrm{ee}}^{-1} + l_{\mathrm{dis}}^{-1}\right)^{-1}$ is dominated by l_{dis}.

Although we are not able to directly map the resistivity with KPFM or EFM, the recorded electric field maps at high doping give a reasonable estimate assuming homogeneous current density I_{SD}/W (I_{SD}: source-drain current, W: sample width) in first order, since non-trivial viscous properties disappear at large $|V_{\mathrm{gate}}|$ (Fig. 5a, main text). This allows to approximately map local variations in resistivity $\rho_{\mathrm{loc}}(x,y) = \frac{\langle E_x^{\mathrm{meas}}(x,y,V_{\mathrm{gate}})\rangle_{V_{\mathrm{gate}}}}{I_{\mathrm{SD}}/W}$ by averaging $E_x^{\mathrm{meas}}(x,y)$ across $V_{\mathrm{gate}} = -141 - -91\,\mathrm{V}$ for each position (Fig. S13a). Averaging instead across a spatial area results in $\overline{\rho}_{\mathrm{local}}(V_{\mathrm{gate}}) = \frac{\langle E_x^{\mathrm{meas}}(x,y,V_{\mathrm{gate}})\rangle_{x,y}}{I_{\mathrm{SD}}/W}$ as shown in Fig. S13b for a few areas and compared to the measured two probe resistivity of the device. While differences appear around charge neutrality, all curves display a largely gate independent similar resistivity for $n \leq -2 \times 10^{17}\,\mathrm{m}^{-2}$.

Independence of resistivity from V_{gate}, respectively from carrier concentration n, is indicative of scattering dominated by short range disorder, while $\rho \propto n^{-1}$ indicates dominant long range disorder scattering.[54] Therefore, we deduce that the former dominates at large hole density. Electron-phonon scattering at longitudinal accoustic phonons results as well in n-independent resistivity,[55] but can be estimated as $\rho_{\mathrm{A}} \approx 30\,\Omega$,[55,73] i.e., much lower than the measured resistivity of $\rho = 500\,\Omega$. Finally, scattering at remote interfacial phonons (polar optical phonons of the substrate) can play a role for graphene at room temperature[54,73] exhibiting a resistivity contribution $\rho_{\mathrm{remote}} \propto \frac{\hbar\omega_{\mathrm{s}}}{e^{\hbar\omega_{\mathrm{s}}/k_{\mathrm{B}}T}-1}$,[74] where ω_{s} is the frequency of the remote surface polar optical phonon being 110 meV for Si_3N_4[75] (59 meV for SiO_2).[73,74] Since the remote phonon contribution on SiO_2 has been measured as $\rho_{\mathrm{remote}} \approx 26\,\Omega$,[73] we get for Si_3N_4: $\rho_{\mathrm{remote}} \approx 26\,\Omega\left(\frac{110\,\mathrm{meV}}{59\,\mathrm{meV}}\right)\frac{e^{59\,\mathrm{meV}/k_{\mathrm{B}}T}-1}{e^{110\,\mathrm{meV}/k_{\mathrm{B}}T}-1} = 5\,\Omega \ll \rho_{\mathrm{A}} \ll \rho_{\mathrm{loc}}$. Thus, the remote phonon contribution can be neglected as well. This implies a dominating scattering at short range defects for large hole doping with scattering length l_{SR}.

To calculate the gate dependence of the resulting $l_{\mathrm{dis}}(E_{\mathrm{F}})$, we use the semiclassical Boltzmann transport equation for the scattering time $\tau(E_{\mathrm{F}}) = l_{\mathrm{dis}}(E_{\mathrm{F}})/v_{\mathrm{F}}$ reading[54]

$$\frac{1}{\rho} = \frac{e^2 v_F^2}{2} D(E_F)\tau(E_F) = \frac{e^2 v_F}{2} D(E_F) l_{dis}(E_F) \tag{S.24}$$

with density of states of graphene $D(E_F) = \frac{4\sqrt{\pi|n(E_F)|}}{h v_F}$. Substituting $D(E_F)$ into eq. (S.24) and solving for l_{dis}, we obtain eq. (5), main text, when using $\rho = \rho_{local}(x, y)$ in order to maintain the spatial character of $l_{dis}(x, y)$ and $n(x, y)$. Figure S13c displays the resulting $l_{dis}(n)$, respectively $l_{dis}(V_{gate})$ using a capacitive model together with its contributions l_{SR} and the electron-phonon contribution $l_{e-ph} \propto 1/\rho_A$ as discussed above. Importantly, l_{dis} increases towards charge neutrality (V_D), oppositely to the behaviour of l_{ee} (eq. (S.23)), such that dominating electron-electron scattering naturally results at low doping.

Comparing Local Scattering Lengths

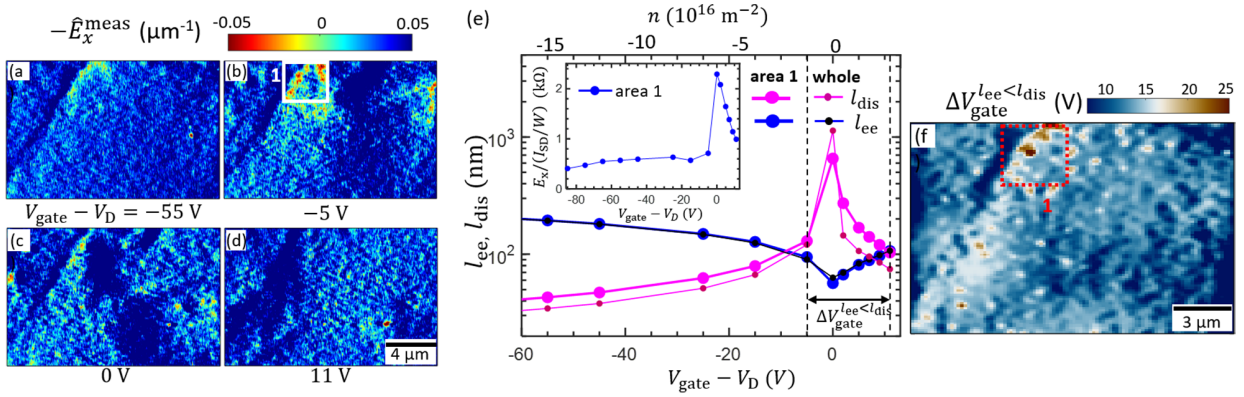

Figure S14: **Comparison of Different Scattering Lengths.** (a–d) $\widehat{E}_x^{meas}(x, y, V_{SD} = 0.5\,V)$ at the mentioned gate voltages (partly shown in Fig. 5, main text), $V_D = 85\,V$. The respective topography is shown in Fig.1f, main text. The white rectangle highlights an area including inverted electric field regions. (e) Dependence on V_{gate} (bottom axis) and carrier concentration (top axis) of electron-electron scattering length l_{ee} (dark lines) and electron-disorder scattering length l_{dis} (pink lines) for the marked area in b (area 1, thick symbols) and the whole area of a–d (thin symbols). Dashed lines labelled $V_{gate}^{l_{ee}<l_{dis}}$ mark the range where $l_{ee} < l_{dis}$ for the thick symbols. Inset: V_{gate} dependence of $\overline{\rho}_{loc}$ for area 1. (f) Map of $V_{gate}^{l_{ee}<l_{dis}}(x, y)$ for the same area as displayed in a–d using a spatial average of $0.2\,\mu m \times 0.2\,\mu m$ for each point (x, y). The rectangle marks the same area as in b.

The ability to map, within the same area, the doping distribution $n_0(x, y)$ and the transport induced electric fields $E_x^{meas}(x, y)$, leading to $\rho_{local}(x, y)$ at high hole doping, allows us

to derive corresponding maps of electron-electron scattering length $l_{\mathrm{ee}}(x, y)$ and electron-disorder scattering length $l_{\mathrm{dis}}(x, y)$ via eq. (4) and eq. (5), main text, respectively. Hence, we are able to locally compare these length scales as shown in Fig. 4g, main text, revealing that inverted electric fields appear preferentially in areas where the V_{gate} range with $l_{\mathrm{ee}} < l_{\mathrm{dis}}$ is largest. In the particular case of Fig. 4, the inverted electric fields appeared on the electron side close to charge neutrality. Here, we add an example, where the inverted fields are observed on the hole side close to charge neutrality (Fig. S14a–d), in particular, at the right of the fold penetrating the whole image (topography: Fig. 1f, main text). This area also shows lowest $E_x^{\mathrm{meas}}(x, y)$ far away from charge neutrality (Fig. S14a) implying low $\rho_{\mathrm{loc}}(x, y)$ and, thus, large $l_{\mathrm{dis}}(x, y)$ (eq. (S.24)), hence, favoring electron viscosity around charge neutrality. In line, again the areas with largest V_{gate} range, where l_{ee} dominates with respect to l_{dis} (Fig. S14e), showcase inverted electric fields as more directly corroborated by mapping the V_{gate} range with $l_{\mathrm{ee}} < l_{\mathrm{dis}}$ directly, called $V_{\mathrm{gate}}^{l_{\mathrm{ee}}<l_{\mathrm{dis}}}(x, y)$ (Fig. S14f) and comparing it with the $E_x^{\mathrm{meas}}(x, y)$ maps of the identical region (Fig. S14a–d).

The inset in Fig. S14e displays $\overline{\rho}_{\mathrm{loc}}(V_{\mathrm{gate}})$ for the highlighted area 1 exhibiting a wide V_{gate} range with constant $\overline{\rho}_{\mathrm{loc}}$. This confirms our previous conclusion of dominating short range disorder scattering for l_{dis}, particularly for the area with inverted electric fields.

Acknowledgement

The authors thank for helpful discussions with K. Sotthewes, C. B. Winkelmann, O. Kolosov, V. Falko, and A. Tzalenchuk. This project has received funding from the European Union's Horizon 2020 research and innovation programme under grant agreement number 881603 (Graphene Core3) as well as the Humboldt foundation via a grant of S.S.

References

(1) Polini, M.; Geim, A. K. Viscous electron fluids. *Phys. Today* **2020**, *73*, 28–34.

(2) Mayzel, J.; Steinberg, V.; Varshney, A. Stokes flow analogous to viscous electron current in graphene. *Nat. Commun.* **2019**, *10*, 937.

(3) Schäfer, T.; Teaney, D. Nearly perfect fluidity: from cold atomic gases to hot quark gluon plasmas. *Rep. Prog. Phys.* **2009**, *72*, 126001.

(4) Narozhny, B. N.; Gornyi, I. V.; Mirlin, A. D.; Schmalian, J. Hydrodynamic Approach to Electronic Transport in Graphene. *Ann. Phys.* **2017**, *529*, 1700043.

(5) Narozhny, B. N. Electronic hydrodynamics in graphene. *Ann. Phys.* **2019**, *411*, 167979.

(6) Torre, I.; Tomadin, A.; Geim, A. K.; Polini, M. Nonlocal transport and the hydrodynamic shear viscosity in graphene. *Phys. Rev. B* **2015**, *92*, 165433.

(7) Gurzhi, R. N. Hydrodynamic effects in solids at low temperature. *Sov. Phys. Usp.* **1968**, *11*, 255–270.

(8) Govorov, A. O.; Heremans, J. J. Hydrodynamic Effects in Interacting Fermi Electron Jets. *Physical Review Letters* **2004**, *92*, 026803.

(9) Guo, H.; Ilseven, E.; Falkovich, G.; Levitov, L. S. Higher-than-ballistic conduction of viscous electron flows. *Proc. Nat. Acad. Sci.* **2017**, *114*, 3068–3073.

(10) Moessner, R.; Morales-Durán, N.; Surówka, P.; Witkowski, P. Boundary-condition and geometry engineering in electronic hydrodynamics. *Phys. Rev. B* **2019**, *100*, 155115.

(11) Holder, T.; Queiroz, R.; Scaffidi, T.; Silberstein, N.; Rozen, A.; Sulpizio, J. A.; Ella, L.; Ilani, S.; Stern, A. Ballistic and hydrodynamic magnetotransport in narrow channels. *Phys. Rev. B* **2019**, *100*, 245305.

(12) Mohseni, K.; Shakouri, A.; Ram, R. J.; Abraham, M. C. Electron vortices in semiconductors devices. *Phys. Fluids* **2005**, *17*, 100602.

(13) Levitov, L.; Falkovich, G. Electron viscosity, current vortices and negative nonlocal resistance in graphene. *Nat. Phys.* **2016**, *12*, 672–676.

(14) Danz, S.; Narozhny, B. N. Vorticity of viscous electronic flow in graphene. *2D Materials* **2020**, *7*, 035001.

(15) Chandra, M.; Kataria, G.; Sahdev, D.; Sundararaman, R. Hydrodynamic and ballistic AC transport in two-dimensional Fermi liquids. *Phys. Rev. B* **2019**, *99*, 165409.

(16) Lent, C. S. Ballistic current vortex excitations in electron waveguide structures. *Appl. Phys. Lett.* **1990**, *57*, 1678–1680.

(17) Pellegrino, F. M. D.; Torre, I.; Geim, A. K.; Polini, M. Electron hydrodynamics dilemma: Whirlpools or no whirlpools. *Phys. Rev. B* **2016**, *94*, 155414.

(18) Mendoza, M.; Herrmann, H. J.; Succi, S. Preturbulent Regimes in Graphene Flow. *Phys. Rev. Lett.* **2011**, *106*, 156601.

(19) Li, S.; Levchenko, A.; Andreev, A. V. Hydrodynamic electron transport near charge neutrality. *Phys. Rev. B* **2020**, *102*, 075305.

(20) Hui, A.; Lederer, S.; Oganesyan, V.; Kim, E.-A. Quantum aspects of hydrodynamic transport from weak electron-impurity scattering. *Phys. Rev. B* **2020**, *101*, 121107.

(21) de Jong, M. J. M.; Molenkamp, L. W. Hydrodynamic electron flow in high-mobility wires. *Phys. Rev. B* **1995**, *51*, 13389–13402.

(22) Bandurin, D. A.; Torre, I.; Kumar, R. K.; Shalom, M. B.; Tomadin, A.; Principi, A.; Auton, G. H.; Khestanova, E.; Novoselov, K. S.; Grigorieva, I. V.; Ponomarenko, L. A.; Geim, A. K.; Polini, M. Negative local resistance caused by viscous electron backflow in graphene. *Science* **2016**, *351*, 1055–1058.

(23) Crossno, J.; Shi, J. K.; Wang, K.; Liu, X.; Harzheim, A.; Lucas, A.; Sachdev, S.; Kim, P.; Taniguchi, T.; Watanabe, K.; Ohki, T. A.; Fong, K. C. Observation of the

Dirac fluid and the breakdown of the Wiedemann-Franz law in graphene. *Science* **2016**, *351*, 1058–1061.

(24) Ghahari, F.; Xie, H.-Y.; Taniguchi, T.; Watanabe, K.; Foster, M. S.; Kim, P. Enhanced Thermoelectric Power in Graphene: Violation of the Mott Relation by Inelastic Scattering. *Phys. Rev. Lett.* **2016**, *116*, 136802.

(25) Gallagher, P.; Yang, C.-S.; Lyu, T.; Tian, F.; Kou, R.; Zhang, H.; Watanabe, K.; Taniguchi, T.; Wang, F. Quantum-critical conductivity of the Dirac fluid in graphene. *Science* **2019**, *364*, 158–162.

(26) Kumar, R. K. et al. Superballistic flow of viscous electron fluid through graphene constrictions. *Nat. Phys.* **2017**, *13*, 1182–1185.

(27) Berdyugin, A. I.; Xu, S. G.; Pellegrino, F. M. D.; Kumar, R. K.; Principi, A.; Torre, I.; Shalom, M. B.; Taniguchi, T.; Watanabe, K.; Grigorieva, I. V.; Polini, M.; Geim, A. K.; Bandurin, D. A. Measuring Hall viscosity of graphene's electron fluid. *Science* **2019**, *364*, 162–165.

(28) Bandurin, D. A.; Shytov, A. V.; Levitov, L. S.; Kumar, R. K.; Berdyugin, A. I.; Shalom, M. B.; Grigorieva, I. V.; Geim, A. K.; Falkovich, G. Fluidity onset in graphene. *Nat. Commun.* **2018**, *9*, 4533.

(29) Geurs, J.; Kim, Y.; Watanabe, K.; Taniguchi, T.; Moon, P.; Smet, J. H. Rectification by hydrodynamic flow in an encapsulated graphene Tesla valve. *arXiv:* **2020**, *2008.04862*.

(30) Lucas, A.; Fong, K. C. Hydrodynamics of electrons in graphene. *J. Phys.: Cond. Matt.* **2018**, *30*, 053001.

(31) Moll, P. J. W.; Kushwaha, P.; Nandi, N.; Schmidt, B.; Mackenzie, A. P. Evidence for hydrodynamic electron flow in PdCoO2. *Science* **2016**, *351*, 1061–1064.

(32) Fu, C.; Guin, S. N.; Scaffidi, T.; Sun, Y.; Saha, R.; Watzman, S. J.; Srivastava, A. K.; Li, G.; Schnelle, W.; Parkin, S. S. P.; Felser, C.; Gooth, J. Largely Suppressed Magneto-Thermal Conductivity and Enhanced Magneto-Thermoelectric Properties in $PtSn_4$. *Research* **2020**, *2020*, 4643507.

(33) Gooth, J.; Menges, F.; Kumar, N.; Süβ, V.; Shekhar, C.; Sun, Y.; Drechsler, U.; Zierold, R.; Felser, C.; Gotsmann, B. Thermal and electrical signatures of a hydrodynamic electron fluid in tungsten diphosphide. *Nat. Commun.* **2018**, *9*, 4093.

(34) Block, A.; Principi, A.; Hesp, N. C. H.; Cummings, A. W.; Liebel, M.; Watanabe, K.; Taniguchi, T.; Roche, S.; Koppens, F. H. L.; van Hulst, N. F.; Tielrooij, K.-J. Observation of giant and tunable thermal diffusivity of Dirac fluid at room temperature. *arXiv:* **2020**, *2008.04189*.

(35) Sulpizio, J. A. et al. Visualizing Poiseuille flow of hydrodynamic electrons. *Nature* **2019**, *576*, 75–79.

(36) Ku, M. J. H. et al. Imaging viscous flow of the Dirac fluid in graphene. *Nature* **2020**, *583*, 537–541.

(37) Jenkins, A.; Baumann, S.; Zhou, H.; Meynell, S. A.; Yang, D.; Watanabe, K.; Taniguchi, T.; Lucas, A.; Young, A. F.; Jayich, A. C. B. Imaging the breakdown of ohmic transport in graphene. *arXiv:* **2020**, *2002.05065*.

(38) Braem, B. A.; Pellegrino, F. M. D.; Principi, A.; Röösli, M.; Gold, C.; Hennel, S.; Koski, J. V.; Berl, M.; Dietsche, W.; Wegscheider, W.; Polini, M.; Ihn, T.; Ensslin, K. Scanning gate microscopy in a viscous electron fluid. *Phys. Rev. B* **2018**, *98*, 241304.

(39) Melitz, W.; Shen, J.; Kummel, A. C.; Lee, S. Kelvin probe force microscopy and its application. *Surf. Sci. Rep.* **2011**, *66*, 1–27.

(40) Xu, J.; Chen, D.; Li, W.; Xu, J. Surface potential extraction from electrostatic and Kelvin-probe force microscopy images. *J. Appl. Phys.* **2018**, *123*, 184301.

(41) Panchal, V.; Pearce, R.; Yakimova, R.; Tzalenchuk, A.; Kazakova, O. Standardization of surface potential measurements of graphene domains. *Sci. Rep.* **2013**, *3*, 2597.

(42) Burnett, T.; Yakimova, R.; Kazakova, O. Mapping of Local Electrical Properties in Epitaxial Graphene Using Electrostatic Force Microscopy. *Nano Lett.* **2011**, *11*, 2324–2328.

(43) Datta, S. S.; Strachan, D. R.; Mele, E. J.; Johnson, A. T. C. Surface Potentials and Layer Charge Distributions in Few-Layer Graphene Films. *Nano Lett.* **2009**, *9*, 7–11.

(44) Altvater, M. A.; Wu, S.; Zhang, Z.; Zhu, T.; Li, G.; Watanabe, K.; Taniguchi, T.; Andrei, E. Y. Electrostatic imaging of encapsulated graphene. *2D Mat.* **2019**, *6*, 045034.

(45) Falkovich, G.; Levitov, L. Linking Spatial Distributions of Potential and Current in Viscous Electronics. *Phys. Rev. Lett.* **2017**, *119*, 066601.

(46) Shaygan, M.; Otto, M.; Sagade, A. A.; Chavarin, C. A.; Bacher, G.; Mertin, W.; Neumaier, D. Low Resistive Edge Contacts to CVD-Grown Graphene Using a CMOS Compatible Metal. *Ann. Phys.* **2017**, *529*, 1–7.

(47) Yu, Y.-J.; Zhao, Y.; Ryu, S.; Brus, L. E.; Kim, K. S.; Kim, P. Tuning the graphene work function by electric field effect. *Nano Lett.* **2009**, *9*, 3430–3434.

(48) Samaddar, S.; Coraux, J.; Martin, S. C.; Grévin, B.; Courtois, H.; Winkelmann, C. B. Equal variations of the Fermi level and work function in graphene at the nanoscale. *Nanoscale* **2016**, *8*, 15162–15166.

(49) Martin, J.; Akerman, N.; Ulbricht, G.; Lohmann, T.; Smet, J. H.; von Klitzing, K.; Yacoby, A. Observation of electron-hole puddles in graphene using a scanning single-electron transistor. *Nat. Phys.* **2007**, *4*, 144–148.

(50) Giuliani, G.; Vignale, G. *Quantum Theory of the Electron Liquid*; Cambridge University Press, 2005; pp 432–439.

(51) Polini, M.; Vignale, G. *No-nonsense Physicist: An Overview of Gabriele Giuliani's Work and Life*; Edizioni della Normale, 2016; Vol. 2; pp 107–124.

(52) Kim, M. et al. Control of electron-electron interaction in graphene by proximity screening. *Nat. Commun.* **2020**, *11*, 2339.

(53) Sheehy, D. E.; Schmalian, J. Quantum critical scaling in graphene. *Phys. Rev. Lett.* **2007**, *99*, 226803.

(54) Sarma, S. D.; Adam, S.; Hwang, E. H.; Rossi, E. Electronic transport in two-dimensional graphene. *Rev. Mod. Phys.* **2011**, *83*, 407–470.

(55) Li, Q.; Sarma, S. D. Finite temperature inelastic mean free path and quasiparticle lifetime in graphene. *Phys. Rev. B* **2013**, *87*, 085406.

(56) Neumaier, D.; Pindl, S.; Lemme, M. C. Integrating graphene into semiconductor fabrication lines. *Nat. Mater.* **2019**, *18*, 525–529.

(57) Ella, L.; Rozen, A.; Birkbeck, J.; Ben-Shalom, M.; Perello, D.; Zultak, J.; Taniguchi, T.; Watanabe, K.; Geim, A. K.; Ilani, S.; Sulpizio, J. A. Simultaneous voltage and current density imaging of flowing electrons in two dimensions. *Nat. Nanotechnol.* **2019**, *14*, 480–487.

(58) Sinterhauf, A.; Traeger, G. A.; Pakdehi, D. M.; Schädlich, P.; Willke, P.; Speck, F.; Seyller, T.; Tegenkamp, C.; Pierz, K.; Schumacher, H. W.; Wenderoth, M. Substrate induced nanoscale resistance variation in epitaxial graphene. *Nat. Commun.* **2020**, *11*, 555.

(59) Li, X.; Zhu, Y.; Cai, W.; Borysiak, M.; Han, B.; Chen, D.; Piner, R. D.; Colombo, L.;

Ruoff, R. S. Transfer of large-area graphene films for high-performance transparent conductive electrodes. *Nano Lett.* **2009**, *9*, 4359–4363.

(60) Adam, S.; Hwang, E. H.; Galitski, V. M.; Sarma, S. D. A self-consistent theory for graphene transport. *Proc. Nat. Acad. Sci.* **2007**, *104*, 18392—-18397.

(61) `https://www.bruker.com/products/surface-and-dimensional-analysis/atomic-force-microscopes/dimension-icon/overview.html`.

(62) Nečas, D.; Klapetek, P. Gwyddion: an open-source software for SPM data analysis. *Central European Journal of Physics* **2012**, *10*, 181–188.

(63) Zerweck, U.; Loppacher, C.; Otto, T.; Grafström, S.; Eng, L. M. Accuracy and resolution limits of Kelvin probe force microscopy. *Phys. Rev. B* **2005**, *71*, 125424.

(64) `https://www.brukerafmprobes.com/p-3950-scm-pit-v2.aspx`.

(65) S.Hudlet,; Jean, M. S.; Guthmann, C.; Berger, J. Evaluation of the capacitive force between an atomic force microscopy tip and a metallic surface. *Eur. Phys. J. B* **1998**, *2*, 5–10.

(66) Strassburg, E.; Boag, A.; Rosenwaks, Y. Reconstruction of electrostatic force microscopy images. *Rev. Sci. Instr.* **2005**, *76*, 083705.

(67) Li, G.; Mao, B.; Lan, F.; Liu, L. Practical aspects of single-pass scan Kelvin probe force microscopy. *Rev. Sci. Instrum* **2012**, *83*, 113701.

(68) Willke, P.; Möhle, C.; Sinterhauf, A.; Kotzott, T.; Yu, H. K.; Wodtke, A.; Wenderoth, M. Local transport measurements in graphene on SiO_2 using Kelvin probe force microscopy. *Carbon* **2016**, *102*, 470–476.

(69) Girard, P. Electrostatic force microscopy: Principles and some applications to semiconductors. *Nanotechnology* **2001**, *12*, 485–490.

(70) Giessibl, F. J. Advances in atomic force microscopy. *Rev. Mod. Phys.* **2003**, *75*, 136802.

(71) Hwang, E. H.; Hu, B. Y.-K.; Sarma, S. D. Inelastic carrier lifetime in graphene. *Phys. Rev. B* **2007**, *76*, 115434.

(72) Sarma, S. D.; Hwang, E. H.; Tse, W.-K. Many-body interaction effects in doped and undoped graphene: Fermi liquid versus non-Fermi liquid. *Phys. Rev. B* **2007**, *75*, 121406(R).

(73) Chen, J.-H.; Jang, C.; Xiao, S.; Ishigami, M.; Fuhrer, M. S. Intrinsic and extrinsic performance limits of graphene devices on SiO_2. *Nat. Nanotechnol.* **2008**, *3*, 206–209.

(74) Fratini, S.; Guinea, F. Substrate-limited electron dynamics in graphene. *Phys. Rev. B* **2008**, *77*, 195415.

(75) Zhu, W.; Neumayer, D.; Perebeinos, V.; Avouris, P. Silicon nitride gate dielectrics and band gap engineering in graphene layers. *Nano Lett.* **2010**, *10*, 3572–3576.

Graphical TOC Entry